Excited states in the exotic nuclei ^{156}Lu and ^{158}Lu

Thesis submitted in accordance with the requirements of the University of Liverpool for the degree of Doctor in Philosophy

by

Christopher Gerard McPeake

Oliver Lodge Laboratory

April 2017

Acknowledgements

My biggest thanks go to Dr. David Joss, my supervisor, for his friendly approach. I really could not have done it without him. He was very supportive in difficult times and I will always be grateful.

I am grateful to Prof. Robert Page for the extra insight he gave me into my work.

I would like to thank Dr. Cath Scholey for all her help in the early stages of my analysis, and for being my unofficial supervisor in Jyväskylä.

Thanks to the STFC for providing the funding for my research and enabling me to live in Finland for a year.

Thanks a lot to Rob and Baha for their help getting me started in my first year.

I would like to thank the Liverpool Nuclear Physics group for all the laughs, drinks, crosswords and support: Mistry, Mark, Joe, Gredley, Alex, John, Liam G and Liam V, Jamie, Faye, Fuad, Simon, Tom and anyone else I have missed on this list - thanks!

I would also like to thank the Jyväskylä Nuclear Spectroscopy group for the brilliant time I had in Finland: Paul, Rauno, Matti, Tuomas, Juha U, Juha S, Janne, Philippos, Mikael, Jan, Sanna, Kalle, Joonas, Jari, Hussam, Ulrika, Pauli and anyone else I have not included!

I am also hugely grateful to Dr. Graham McDonald at the University of Salford for getting me up to scratch on maths - otherwise I am sure this PhD would not

have been possible.

I would hugely like to thank my family for all their support during difficult times I have had over the last few years. I would also like to thank all my other friends that I have not mentioned above.

Abstract

Excited states in the neutron-deficient odd-odd nuclei ^{156}Lu and ^{158}Lu have been identified using the JUROGAM II and GREAT spectrometers in conjunction with the RITU gas filled separator at the University of Jyväskylä Accelerator Laboratory. The nuclei were populated with the reaction ^{58}Ni + ^{106}Cd $\rightarrow$ ^{164}Os* at a beam energy of 318 MeV with an average beam intensity of 7 pnA provided by the K130 cyclotron. The recoil-decay tagging technique was used to differentiate ^{156}Lu γ-rays from background using JUROGAM II and GREAT, whereas the recoil-isomer tagging technique was used for determining ^{158}Lu γ rays. There was no level scheme known in ^{158}Lu and only 12 states known in ^{156}Lu. A previously undiscovered 19^- isomer has been found in ^{156}Lu. The new ^{156}Lu level scheme has been populated up to 33^+ and the new ^{158}Lu level scheme to 21^-.

Contents

List of Figures

Chapter 1

Introduction

The properties of the atomic nucleus are difficult to predict exactly from the mutual interactions between all its constituent nucleons. A favoured method for making the many-body problem of A interacting nucleons tractable is to adopt models utilising a mean-field approximation incorporating an effective interaction. Such approximations are reflected in the choice of realistic nuclear potentials in the Hamiltonian of the Schrödinger Equation. These potentials allow the relative excitation energies of excited states to be predicted. However, the chosen potential may not always reflect the subtleties of the underlying interactions between nucleons - particularly at extreme proton - neutron number ratios.

One of the main topics of contemporary interest in nuclear structure physics concerns the limits to nuclear existence. The proton drip line represents the locus of points on the nuclear chart where the proton separation energy changes sign and proton radioactivity becomes a possible decay mode. Thus, for odd-Z nuclei, the proton drip line represents a limit beyond which the half-lives of nuclear ground and low-lying isomeric states decrease rapidly. In heavy odd-odd nuclei near closed shells isomeric configurations with relatively long γ-decay lifetimes can be formed by specific single-particle couplings. In proton unbound nuclei such isomers may

potentially have measurable proton emission branches. There is an alternative and exciting possibility that nuclear isomers may extend the limits of observable nuclei beyond the proton drip line. Recent work on the doubly odd nucleus ^{158}Ta, which is proton unbound in its ground state has revealed a 19^- isomeric state that is robust against proton decay, despite being almost 3 MeV proton unbound. Which of these two scenarios is favoured is highly sensitive to the proton radioactivity Q-values and the orbital angular momentum of the emitted proton; small changes in either Q-value or orbital angular momentum could result in orders of magnitude difference in the proton decay half-lives [1].

Precise theoretical predictions for proton emission candidates are challenging and require detailed information on the excitation level schemes in the mother and daughter nuclei. However, such data is often limited in doubly odd nuclei since their level schemes are very complicated reflecting the large number of potential angular momentum couplings of single particles available to produce excited states.

Figure 1.1 shows the chart of nuclides with each square defining a nucleus with a unique combination of Z protons and N neutrons. In addition to the ~300 stable nuclei there are several thousand radioactive species that can be produced via fission or the fusion of accelerated ion beams with stationary targets. There are potentially a large number of exotic nuclei that can be used to test theories. An important constraint on different model approaches, which may change at extreme isospin, is provided by the experimental measurement of excited states from which an understanding of their underlying configurations is possible.

This thesis reports the results of in-beam and decay spectroscopy experiments focusing on the exotic nuclei ^{156}Lu and ^{158}Lu using the JUROGAM II and GREAT spectrometers in conjunction with the RITU gas-filled separator at the Jyväskylä Accelerator Laboratory. These doubly odd nuclei lie close to both the proton drip line and the $N = 82$ shell gap where the spins of excited states are anticipated

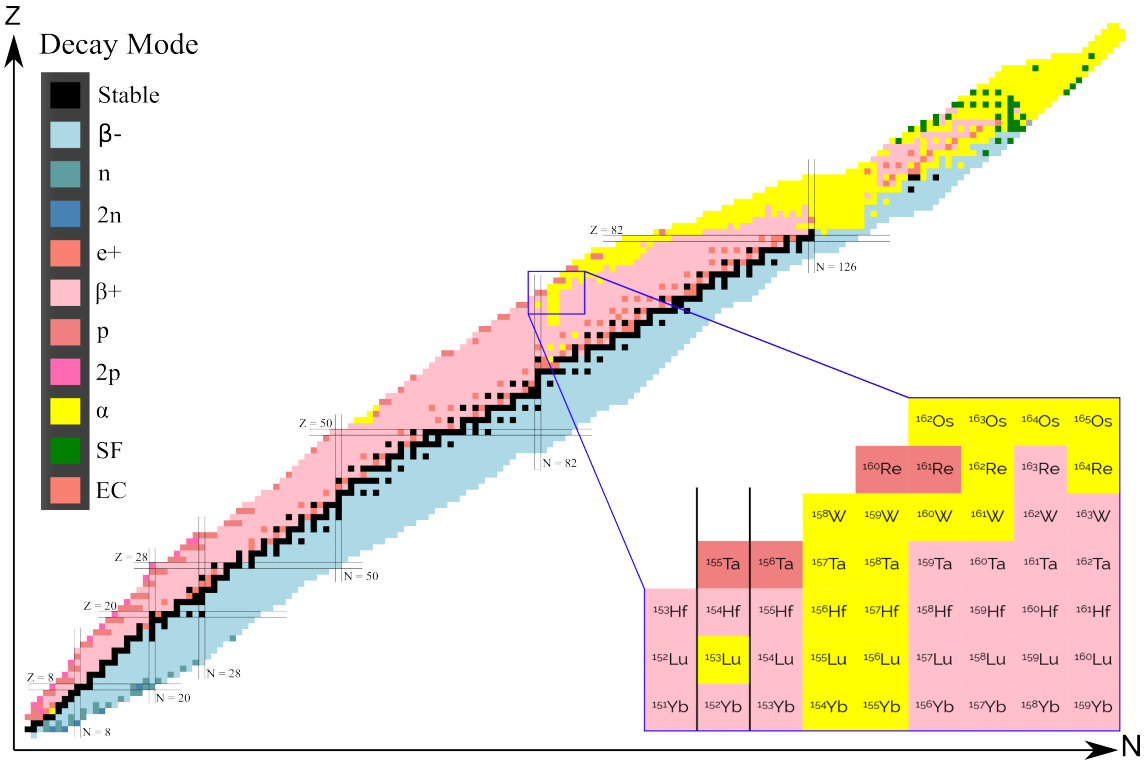

Figure 1.1: The chart of nuclides. The legend assigns colours to indicate the dominant ground-state decay mode. The region of interest around ^{156}Lu and ^{158}Lu is enlarged. [2]

to be generated by the successive alignment of a small number of valence nucleons. Thus, the identification of excited states provides an important benchmark for model predictions of configurations in heavy neutron-deficient nuclei.

The nucleus ^{156}Lu has a 100% α decay branch, which allows γ rays to be identified using the Recoil Decay Tagging (RDT) technique [3]. A level scheme of excited states in ^{156}Lu was established by Ding *et al.* [4] see Figure 1.2. The level scheme for ^{156}Lu has been extended significantly with 18 new transitions including an isomeric state that was measured to have a half-life of 120(17) ns. The nucleus ^{158}Lu is less suitable for RDT studies due to the low α-decay branching ratio (b_α=0.91%) and long half-life ($t_{1/2}$=10.6(3) s). Instead, γ rays were assigned to ^{158}Lu using the LISA spectrometer located at the target position to select transitions associated with the 5 proton fusion-evaporation channel. A level scheme was constructed for the first

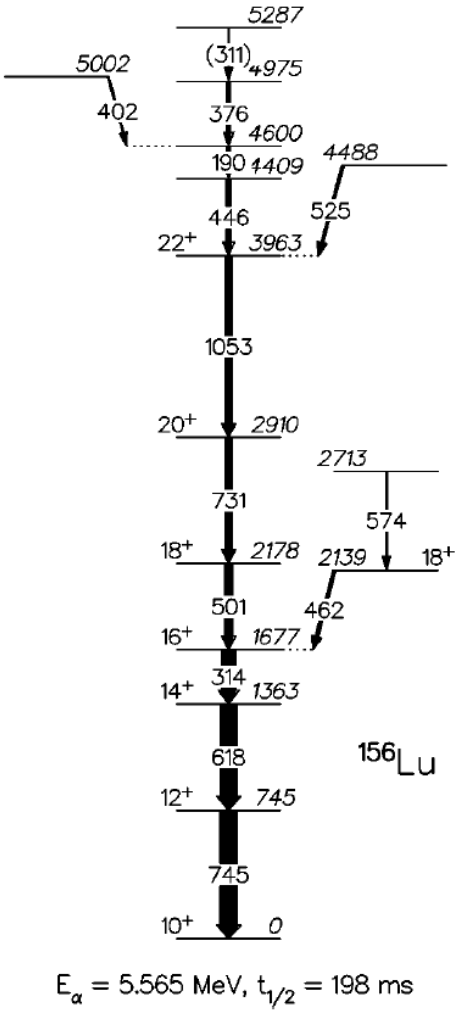

Figure 1.2: Level scheme for ^{156}Lu above the 10^+ state in ^{156}Lu deduced from the experiment of Ding *et al.* [4].

time. This scheme included an isomeric state measured to have a half-life of 456(2)ns and its decay path identified through isomer-decay correlations.

The main focus of this work is to establish or extend the level excitation schemes in the odd-odd Lu nuclei near the proton drip line. Spectroscopic studies of the isotopes ^{156}Lu and ^{158}Lu have been performed using the JUROGAM II and GREAT spectrometers in conjunction with the RITU gas-filled separator. While the nucleus ^{158}Ta is the lightest $N = 85$ isotone that is proton unbound in its ground state

there is still a possibility that excited states in ^{156}Lu (S_p=540 keV) [5] and ^{158}Lu (S_p=1076 keV) [5] might be unbound to proton emission. Prior to this work no excitation scheme had been established for ^{158}Lu.

The thesis introduces the background concepts relevant to the interpretation of the data (Chapter 2) and discusses the experimental apparatus and methodologies exploited in the experimental work (Chapter 3) before reporting the results and interpretation (Chapter 4).

Chapter 2

Concepts in Nuclear Physics

The nucleus contains protons and neutrons that are held together at close proximity by the strong nuclear force, overcoming the repulsion of the Coulomb interaction between the protons. Nuclei can contain from one, to hundreds of nucleons that interact strongly with their nearest neighbours, but weakly with any nucleons at distances greater than $\approx 10^{-15}$ m. Due to the highly complex nature of nuclei, calculations involving single particle interactions of heavy nuclei would be impossible with computing power available today, therefore deliberately simplified mathematical models have to be introduced.

2.1 Nuclear Models

The most basic requirements for a model is that it supports nuclear properties found in past experiments, but also it must be able to predict properties measured in new experiments. The liquid-drop model is one of the simplest nuclear models and it compares the nucleus to a drop of liquid. This model was successful in describing large scale properties of the nucleus such as nuclear fission, and was used to predict binding energies with the semi-empirical mass formula, but fails to explain more

detailed nuclear properties. The semi-empirical mass formula [6], formulated by Carl Friedrich von Weizsäcker in 1935, expresses the binding energy in terms of volume and surface, charge, and the quantum effects of asymmetry and pairing so that

$$B_E(A,Z) = a_v A \; - \; a_s A^{2/3} \; - \; a_c Z(Z \; - \; 1)A^{-1/3} \; - \; a_{sym}\frac{(A \; - \; 2Z)^2}{A} \; + \; \delta, \quad (2.1)$$

where the a_v, a_s, a_c, and a_{sym} coefficients are related to the volume, surface, Coulomb and asymmetry terms, respectively. The pairing term δ can be positive, zero or negative for even-even, odd-even or odd-odd nuclei, respectively.

The energy required to remove a nucleon from the nucleus is known as the proton or neutron separation energy. As the number of protons increases with respect to the number of neutrons, the proton separation energy decreases and the neutron separation energy increases and vice versa. 'Magic numbers' of nucleons (where N or Z = 2, 8, 20, 28, 50, 82 and 126) are similar to the filled electron shells in atomic physics. The separation energies greatly increase at these magic numbers.

2.1.1 The Spherical Shell Model

In the independent particle nuclear shell model [7, 8, 9], individual nucleons have to be seen as moving in a mean field potential, instead of being dealt with as individual particles. Due to this assumption it limits nucleons to only exist in discrete energy levels, or shells, which are separated by energy gaps in a similar way to how electrons occupy shells around the nucleus in the atom, as mentioned in the previous section.

The harmonic oscillator potential was chosen first and can give a reasonably good solution to many analytical problems [10] and has the form

$$V(\mathbf{r}) = \frac{1}{2}\, k\, \mathbf{r}^2 = \frac{1}{2}\, m\, w^2\, \mathbf{r}^2, \tag{2.2}$$

where k is the classical spring constant, $\mathbf{r}$ is the three-dimensional position coordinate, m is the mass and ω is the harmonic oscillator frequency. The nuclear Hamiltonian has to then be combined with the previous equation to describe the energy of the system

$$H(\mathbf{r}) = -\frac{\hbar}{2m} \bigtriangledown^2 + V(\mathbf{r}), \tag{2.3}$$

where the energy eigenvalues correspond to

$$E_N = (N + \tfrac{3}{2})\hbar\omega, \tag{2.4}$$

where N is a quantum number denoting the level [10]. A problem with this model is that the nuclear potential $V(r)$ tends toward infinity, which is known to be an unrealistic factor, as this would mean an infinite amount of energy would be needed to remove the nucleons from the potential well. Experimentally, a more realistic nuclear potential should not be infinite due to a finite surface thickness, so a more accurate interpretation should lie somewhere between the square well and harmonic oscillator potentials, which is why only the first three magic numbers predicted by the Harmonic Oscillator potential match experiments, as shown in Figure 2.1. Another problem with this model is that the energy levels are 'degenerate', meaning multiple eigenstates have the same energy, and the number of degenerate states account for the amount of nucleons that can fill the levels. The reason why this is a problem can be seen by considering the subshells *3s*, *2d*, and *1g* (where $l = 4$, *2*, and *0*) in the $N = 4$ shell are all degenerate.

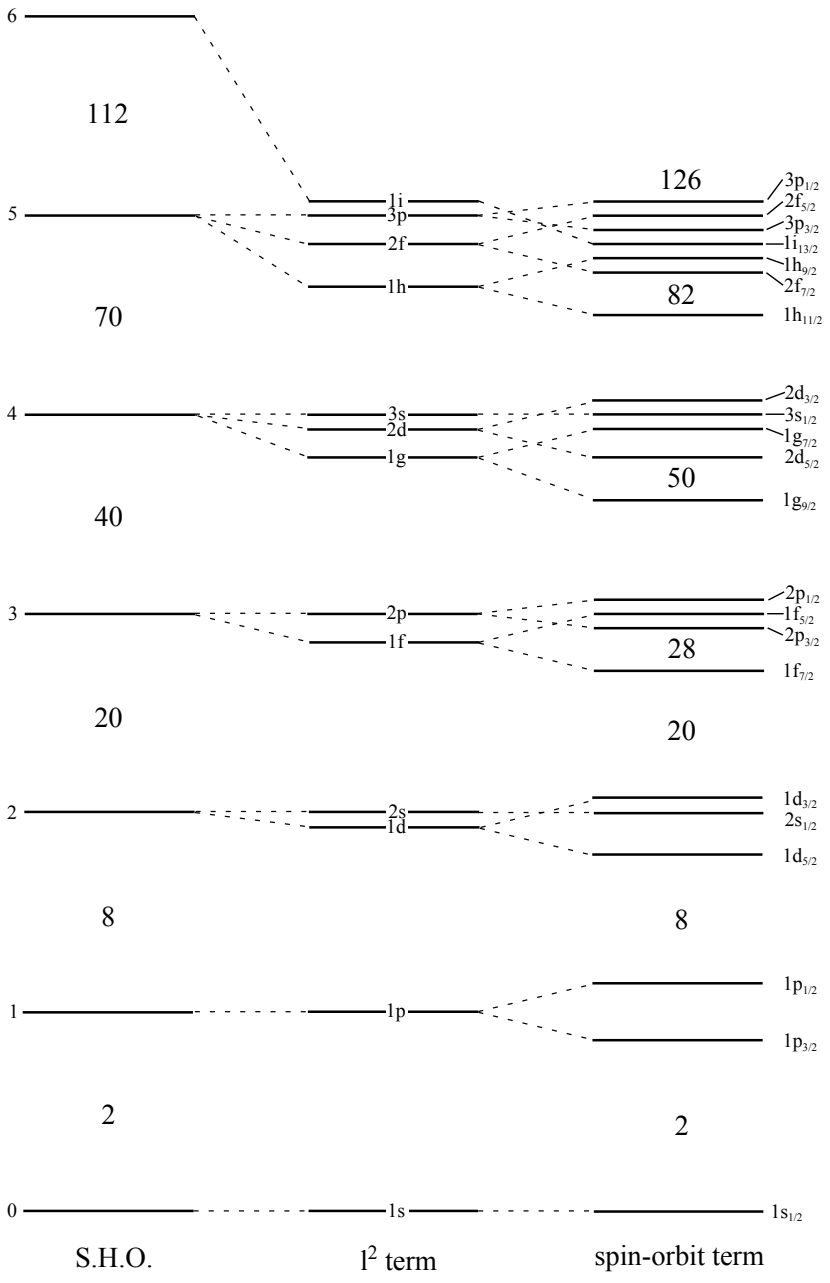

Figure 2.1: A comparison between the more basic Simple Harmonic Oscillator model, and the much improved model due to the spin-orbit term being included.

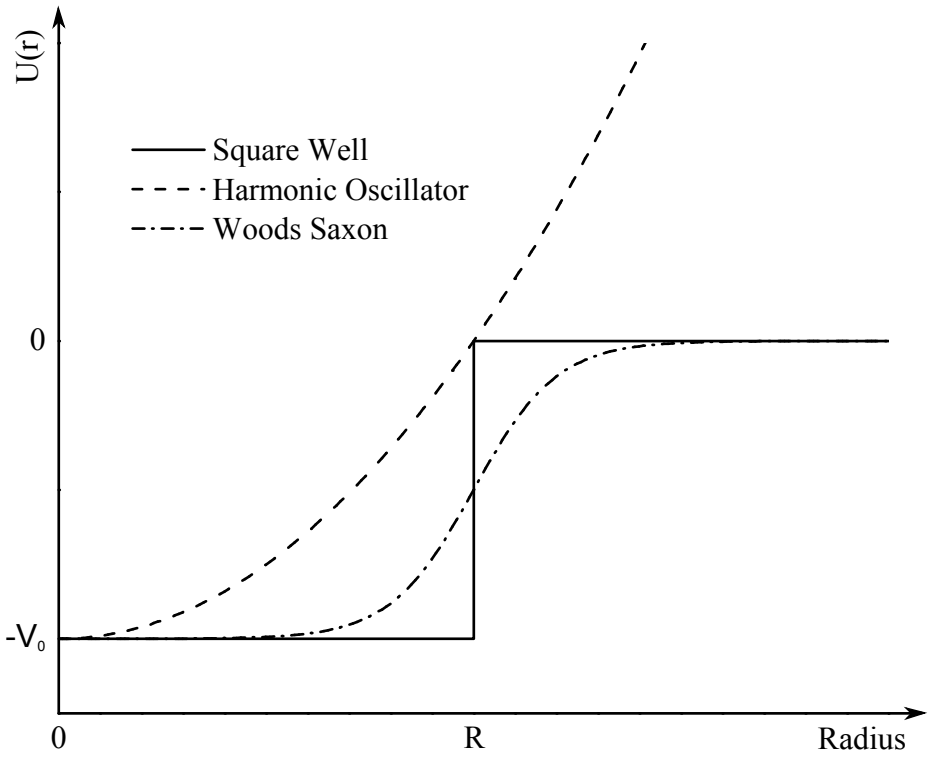

Figure 2.2: Nuclear force potentials using theoretical values. The Woods-Saxon potential combines the square-well and harmonic-oscillator potentials into a more realistic model.

The Woods-Saxon potential is more refined than the harmonic oscillator potential, and can be defined as

$$V(r) = \frac{-V_0}{1 + exp[(r - R)/a]}, \tag{2.5}$$

where r is the distance from the centre of the nucleus, R is the nuclear radius, V_0 is the well depth and a is the diffuseness term that varies with the sharpness of the transition between V_0 and *0*. Typical values for these are $V_0 \approx 50$ MeV, $R = 1.25\mathrm{A}^1/3$ and $a = 0.524$ fm. This allows the level degeneracy to be removed but still does not provide the correct magic numbers at higher levels. It is here where the developments of Mayer and Haxel [7, 8, 9] in spin-orbit coupling become very important. The influence of these corrections on the single-particle energies is shown in Figure 2.2.

2.1.2 The Deformed Shell Model

The deformed shell model, also known as the Nilsson model is one of the most successful nuclear models that has been developed so far [11]. This model predicts single-particle energies and is useful for nearly all deformed nuclei. It is, however, difficult to describe the characteristics of nuclei with very high rotation velocities and in these cases experimentalists have chosen to look only towards single-particle motion. In nuclei that have closed, or nearly closed shells, their shape (at low excitation energies) is typically near-spherical, and can be treated by the spherical independent-particle shell model. Further away from these closed shells is when collectivity develops, and towards the mid-shell regions, the Nilsson model becomes essential to describe their structure shown in Figure 2.3 for neutrons and Figure 2.4 for protons.

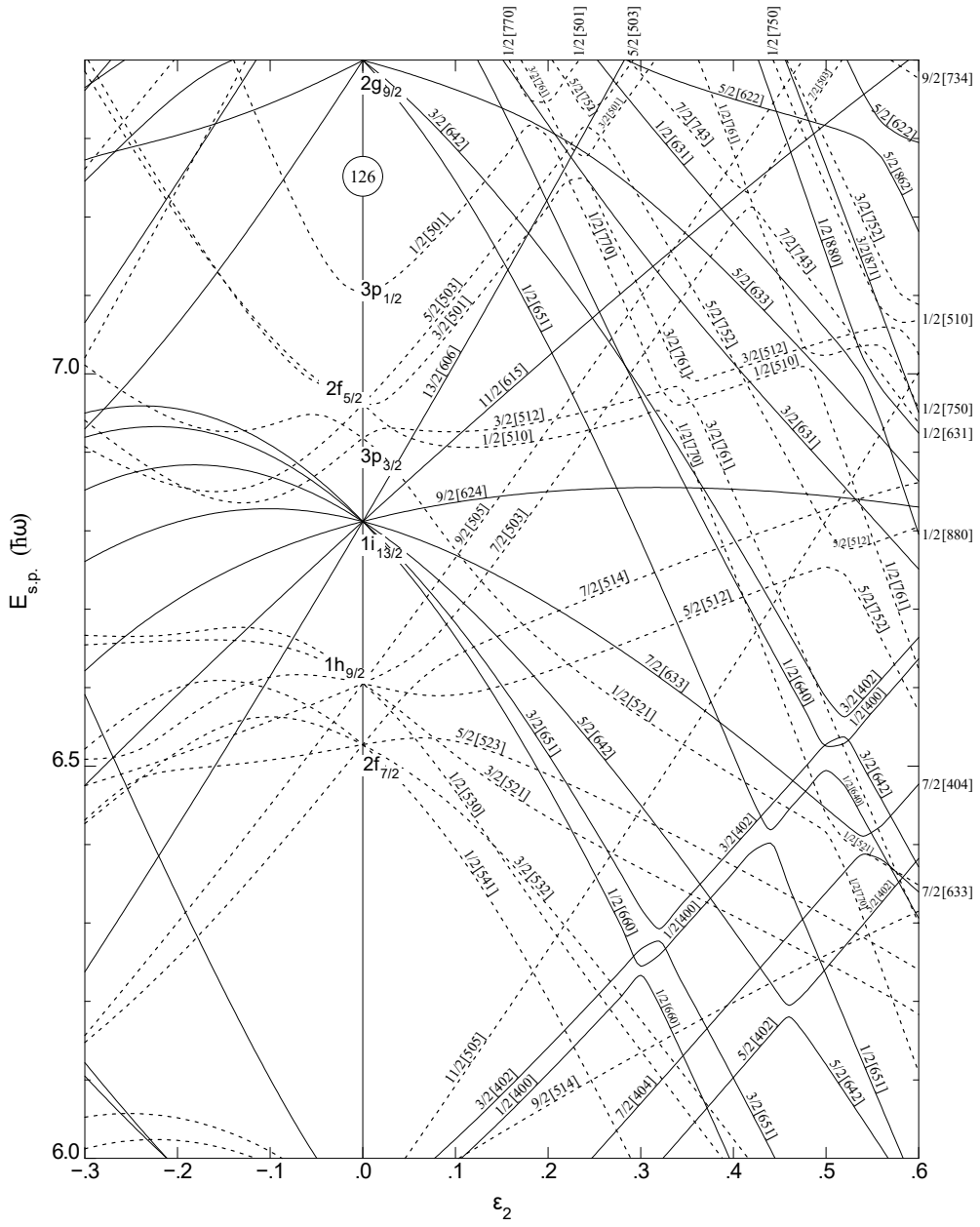

Figure 2.3: Nilsson diagram for neutrons, $82 \leq Z \leq 126$ ($\epsilon_4 = \epsilon_2^2/6$). [2]

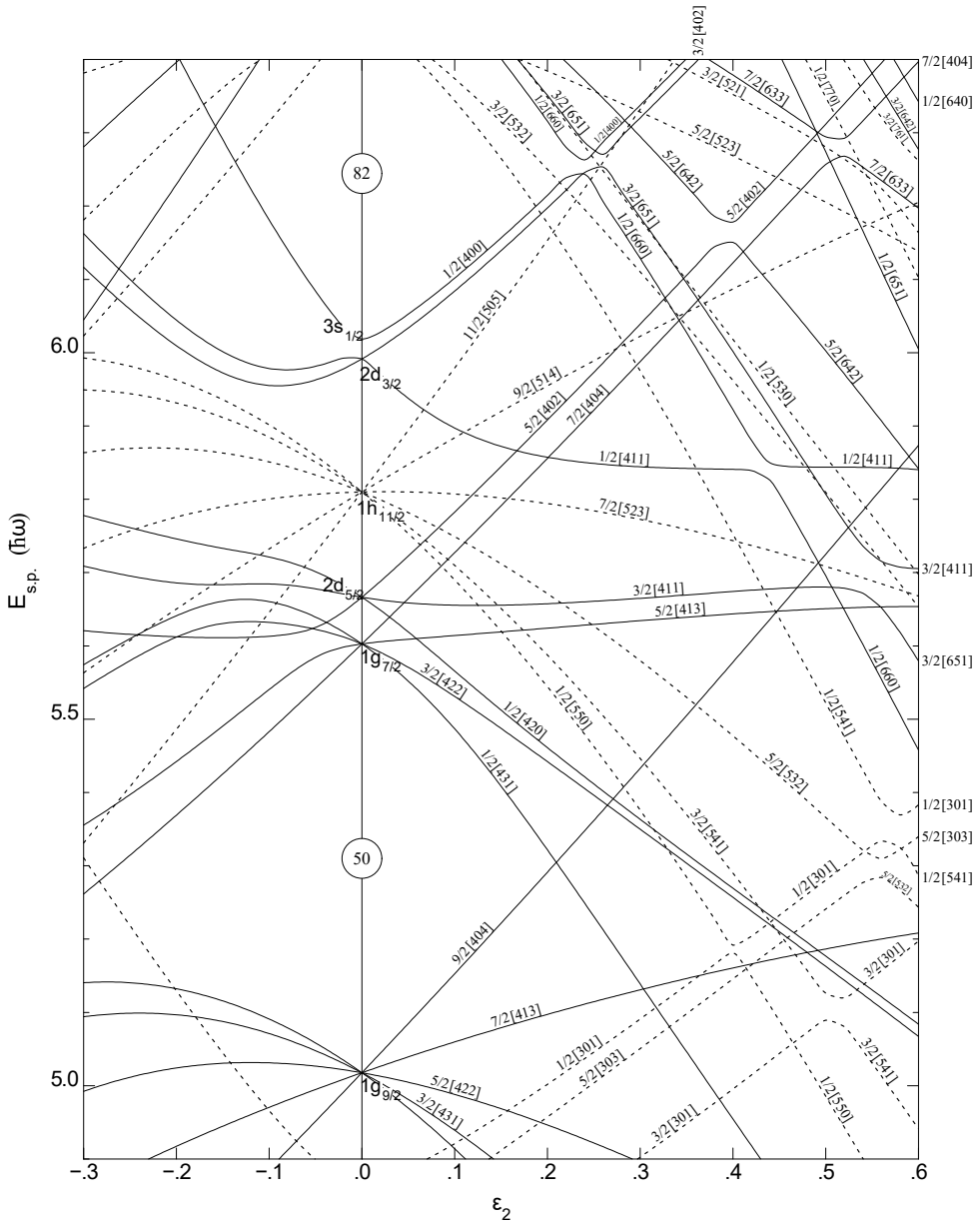

Figure 2.4: Nilsson diagram for protons, $50 \leq Z \leq 82$ ($\epsilon_4 = \epsilon_2^2/6$). [2]

2.1.3 Nuclear Deformation and Rotation

Deformation

Nuclei that are further from closed shells and with significant proton-neutron valence products are susceptible to quadrupole deformation due to the configuration mixing and shifts from the spherical symmetry. The nuclear shape is therefore shifted from spherical to ellipsoidal shapes as a result of the pairing forces from proton-neutron interactions in specific orbitals. The nuclear shape is defined in polar coordinates as

$$R(\theta,\phi) = R_0\left[1 + \alpha_{00} + \sum_{\lambda=1}^{\infty}\sum_{\mu=-\lambda}^{\lambda}\alpha_{\lambda_\mu}Y_\lambda^\mu(\theta,\phi)\right], \tag{2.6}$$

where the radius $R(\theta,\phi)$ of the nucleus is expanded into spherical harmonics Y_λ^μ, and α_{00} constrains the nucleus to have a constant volume. R_0 is the radius of a spherical nucleus with the same volume and α_{λ_μ} are the Hill-Wheeler coordinates [12] that define the deformity away from the equilibrium spherical shape. λ corresponds to the multipolarity, for instance $\lambda = 0$ and 1 for monopole and dipole moments, and $\lambda = 2, 3, 4$ for quadrupole, octupole and hexadecapole degrees of freedom, respectively.

2.1.4 Electromagnetic Transitions

Fusion-evaporation reactions are used to create highly excited nuclei which then decay via electromagnetic transitions, producing structural information about the decaying nucleus from the radiation detected. There are two main electromagnetic processes that allow the excited nuclei to lose energy, and by understanding how these processes work is essential to learning information about the nuclear structure. These processes are γ-ray transitions and internal conversion.

γ Decay

The energies of emitted γ rays provides insight into the excited nucleus by revealing nucleon arrangements. These γ rays are released to reduce the energy and angular momentum of the nucleus. The order in which these γ rays are released provides valuable information about the structure, which can be presented in the form of a level scheme.

The release of γ rays is to allow the nucleus to obey the conservation laws while it is transitioning between the initial and final states. When a nucleus undergoes a transition, most of the energy is released in the emitted γ-ray photon, while a small amount of energy (less than 5 meV) is transferred to the nucleus to preserve momentum of the γ ray that has been emitted. Parity must also be conserved during this transition. This transitioning from one state to another can be viewed as

$$E_\gamma \simeq E_i - E_f, \tag{2.7}$$

where E_i and E_f correspond to the excitation energies of the initial and final states. Similarly, the angular momentum, $\vec{I}$ at its initial and final states of the transition coupled with $\vec{L}$, the multipolarity, shows the angular momentum taken from the nucleus during the transition, which must also be conserved,

$$\vec{L} = \vec{I_i} - \vec{I_f}. \tag{2.8}$$

A relationship can then be made between the multipolarity and the initial and final states of the angular momentum as

$$|I_i - I_f| \leqslant L \leqslant I_i + I_f, \tag{2.9}$$

where the lowest multipole is the dominating one. The mulipolarity of the radiation

Table 2.1: Selection rules for electric and magnetic radiation depending on parity of initial and final states.

$\lvert I_i - I_f \rvert$	1	2	3	4	5	...
No change of parity	M1	E2	M3	E4	M5	...
Change of parity	E1	M2	E3	M4	E5	...

can either be magnetic (M), or electric (E) depending on parity changes between the initial and final states. For an initial and final state that retain the same parity, the radiation will have an *odd* magnetic, or an *even* electric multipolarity, and vice versa, as can be seen in the selection rules in Table 2.1. $M0$ is not a possible transition as magnetic monopoles do not exist in nature, and due to photons carrying at least one unit of angular momentum, $E0$ transitions cannot be the result of γ-ray emission.

Lower order multipole transitions dominate during de-excitation and magnetic transitions are hindered compared to their corresponding electric transitions. Table 2.2 lists the Weisskopf estimates for the first five orders of multipolarity of electric and magnetic transitions.

Table 2.2: Half-lives based on Weisskopf estimates for electric and magnetic transition for the first five orders of multipolarity [13], where A is the mass number and E_γ is the γ-ray energy in MeV.

L	T_{elec} (s)	T_{mag} (s)
1	$6.73\ A^{-2/3}\ E_\gamma^{-3} \times 10^{-15}$	$2.24\ A^{0}\ E_\gamma^{-3} \times 10^{-14}$
2	$9.37\ A^{-4/3}\ E_\gamma^{-5} \times 10^{-9}$	$3.12\ A^{-2/3}\ E_\gamma^{-5} \times 10^{-8}$
3	$1.98\ A^{-2}\ E_\gamma^{-7} \times 10^{-2}$	$6.60\ A^{-4/3}\ E_\gamma^{-7} \times 10^{-2}$
4	$6.30\ A^{-8/3}\ E_\gamma^{-9} \times 10^{4}$	$2.10\ A^{-2}\ E_\gamma^{-9} \times 10^{5}$
5	$2.83\ A^{-10/3}\ E_\gamma^{-11} \times 10^{11}$	$9.43\ A^{-8/3}\ E_\gamma^{-11} \times 10^{11}$

Internal Conversion

Transitions between states that both have a spin and parity of 0^+ are not forbidden, but they cannot decay by single γ-ray emission. Instead the nucleus loses its excess energy by emitting one of its deeply bound atomic electrons. The electron is emitted with the kinetic energy of E_k

$$E_k = (E_i - E_f) \ - \ B_e, \tag{2.10}$$

where E_i and E_f are the excitation energies of the initial and final states with B_e being the electron binding energy, which varies according to the orbital. Once the electron has been emitted, an electron from a higher orbital fills the lower orbital's vacancy, leading to the emission of an X-ray, which can be detected in coincidence with the conversion electrons. At low energy transitions there exists a competition between internal conversion and γ-ray emission and can be expressed as the internal conversion coefficient, α_{icc}, which is defined as a ratio of transition probabilities from internal conversion, λ_e, or γ-ray emission, λ_γ

$$\alpha_{icc} = \frac{\lambda_e}{\lambda_\gamma}, \tag{2.11}$$

with a small value representing when internal conversion is negligible and a large value for when it dominates. The total transition probability, λ, takes into account both internal conversion and γ-ray emission and can be shown as

$$\lambda = \lambda_e + \lambda_\gamma = \lambda_\gamma(1 + \alpha). \tag{2.12}$$

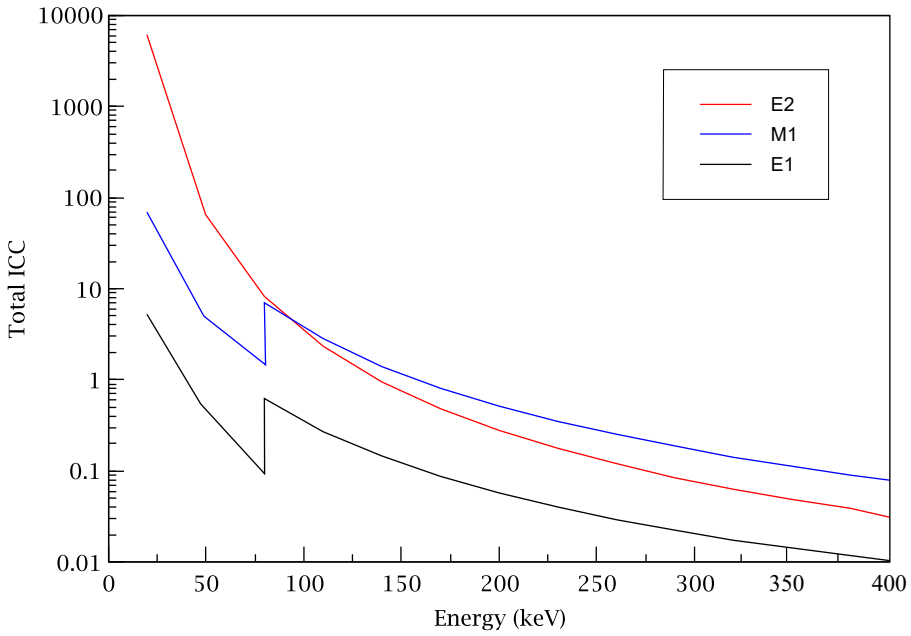

Figure 2.5: Calculated conversion coefficients for E1, E2 and M1 decays in Lu [14].

Transition multipolarity affects internal conversion and ratios can be made between the K, L and M orbitals. The total conversion coefficient can be found by addition of each atomic orbital

$$\alpha = \alpha_K + \alpha_L + \alpha_M + \dots \ . \tag{2.13}$$

Figure 2.5 shows the calculated conversion coefficients for E1, E2 and M1 decays in Lu using BrIcc for the energy range of 20 keV to 400 keV [14].

2.1.5 α Decay

α decay is useful for identifying nuclei due to the distinct decay energies of α particles. The α particle is a strongly bound system that is identical to a ^{4}He nucleus and this allows energy to be released in an effective way. α decay has to be explained with a non-classical explanation and Gamow's [15] theory on α decay, then followed by Gurney and Condon [16], have been the most successful. In the Gamow model

the α particle leaves the parent nucleus by penetrating through the Coulomb barrier in a process known as *quantum tunnelling* and energy, Q_α, is released such that

$$ {}^{A}_{Z}\mathrm{X}_{N} \rightarrow {}^{A-4}_{Z-2}\mathrm{Y}_{N-2} \; + \; \alpha \; + \; Q_\alpha, \tag{2.14} $$

where Z and A are the proton and mass numbers, respectively. Energy is also released in the α decay and the net energy is called the Q_α value, which corresponds to the total kinetic energy of the daughter nucleus and the α particle.

As the half-life of a decay is highly dependent on the Q_α energy, only small differences in alpha-decay energies are needed to produce half-lives with large orders of magnitude differences. In an experiment performed by Geiger and Nuttall [17], the stopping distance of alpha particles in air was measured. They discovered that the decay constant, plotted against the stopping distance of several isotopes, gives a relatively straight line. From this observation, a relationship between the range and the energy of the alpha particles was found

$$ \tau_{1/2_i} \approx a + \frac{b}{\sqrt{Q_\alpha}}, \tag{2.15} $$

where a and b are empirically measured constants that differ depending on the chemical element.

The probability that there will be the emission of an α particle from a nucleus is

$$ P = P_{preform} \; . \; P_{tunnel} \; . \; \nu, \tag{2.16} $$

where $P_{preform}$ is the probability of an α particle existing inside the parent nucleus, P_{tunnel} is the probability the α will quantum mechanically tunnel through the Coulomb barrier and ν is the knocking frequency. $P_{preform}$ is related to the half-life of the decay, while P_{tunnel} can be calculated using Coulomb barrier models, for example

$$P_{tunnel} = exp\ [-2G], \tag{2.17}$$

where G is the Gamow factor shown by

$$G = \sqrt{\frac{2m}{\hbar^2}} \int_a^b \sqrt{V(r) - Q_\alpha}\ dr, \tag{2.18}$$

where a and b are the inner and outer turning points and $V(r)$ is the barrier height.

When writing Equation 2.17 in terms of 2.18

$$P = exp\left[-2\sqrt{\frac{2m}{\hbar^2 Q_\alpha}\ \frac{2Ze^2}{4\pi\epsilon_0}}\left(arccos\sqrt{x} - \sqrt{x(1-x)}\right)\right], \tag{2.19}$$

where $x = a/b$.

This allows the barrier penetration probability to be expressed as [18],

$$P = exp\left[-\int_a^b \frac{\sqrt{2\mu}}{\hbar}\sqrt{V(r)\ +\ \frac{2Ze^2}{r}\ +\ \frac{\hbar^2}{2\mu r^2}l(l+1) - Q_\alpha}\right]\ dr, \tag{2.20}$$

due to the tunnelling probability being highly dependent on the α particle's orbital angular momentum, the atomic number and energy, and where μ is the reduced mass.

Chapter 3

Experimental Methodology

In γ-ray spectroscopy there are many experimental challenges to overcome, stemming from the highly precise methods that are needed in order to synthesise and perform measurements of the nuclei of interest. This chapter discusses in detail topics ranging from the detectors used to the data preparation required for the analysis.

3.1 Exotic Nuclei Synthesis

Heavy-ion fusion-evaporation reactions are suitable for synthesising the nucleus in a high-spin excited state. A fusion-evaporation reaction involves a projectile nucleus which is the beam B fusing with a stationary target nucleus T, resulting in a highly energetic compound nucleus C. The compound nucleus is highly excited due to the large amount of energy that is required for the projectile to overcome the Coulomb barrier of the target nucleus. This reaction can be expressed as

$$ {}^{A_1}_{Z_1}B \; + \; {}^{A_2}_{Z_2}T \; \rightarrow \; {}^{A_1+A_2}_{Z_1+Z_2}C^* \tag{3.1} $$

where A and Z are the mass number and proton number, respectively.

At the University of Jyväskylä, a beam of accelerated ions are fired upon a fixed target located inside the JUROGAM II High-Purity Germanium detector array. The beam and target nuclei fuse into a compound nucleus, in which, a large amount of kinetic energy and angular momentum is transferred. Particle evaporation of the compound nucleus begins due to the highly unstable nature of the system. In order for the compound nucleus to lose energy it "boils off" nucleons or α particles until the system has less excitation energy than the particle separation energy. This happens within a time scale of the order of 10^{-19} s. At this stage the system is close to the yrast line, and any further particle evaporation is not possible. The yrast line is at the locus of density points the maximum angular momentum for a given excitation energy. The remaining excitation energy and angular momentum is dissipated by a cascade of electromagnetic transitions as the residual nucleus travels down the yrast line, see Figure 3.1. "Yrast" comes from the Swedish word meaning "dizziest" and is the highest angular momentum.

For a given excitation energy, fusion-evaporation reactions can be written schematically as

$$^{A_1+A_2}_{Z_1+Z_2}\mathrm{C}^* \rightarrow ^{A_C-(x+y+4z)}_{Z_C-(x+2z)}\mathrm{R} \; + \; xp \; + \; yn \; + \; z\alpha, \tag{3.2}$$

where $A_C = A_1 + A_2$ and $Z_C = Z_1 + Z_2$, which can be written more conventionally as

$$^{A_1}_{Z_1}\mathrm{T}(^{A_1}_{Z_1}\mathrm{B}, xpynz\alpha)^{A_3}_{Z_3}\mathrm{R}, \tag{3.3}$$

where xp is the number of evaporated protons, yn is the number of evaporated neutrons, $z\alpha$ is the number of evaporated α particles, and R is the remaining evaporation residue i.e. the recoil.

The compound nucleus energy is defined as

$$E^* = E_{com} \ + \ Q = \frac{1}{2}\mu\nu_{rel}^2 \ + \ (M_B \ + \ M_T \ - \ M_C)c^2 \tag{3.4}$$

where $\mu = (M_T M_B)/M_C$ is the reduced mass, E_{com} is the centre of mass kinetic energy, Q is the mass difference energy gained, $M_{B,T,C}$ are the beam, target and compound nuclear mass, respectively, and ν_{rel} is the relative velocity. As the target is in a stationary position then the formula can be re-arranged as

$$E^* = E_{com} \ + \ Q = \frac{M_T}{M_B \ + \ M_T}E_B \ + \ (M_B \ + \ M_T \ - \ M_C)c^2, \tag{3.5}$$

where E_B is the kinetic energy of the beam. Monte Carlo simulations can be performed to give an indication of the cross sections of nuclei that will be produced. A beam energy can then be selected in order to populate high or low spin states, depending on what is required by the experiment [19].

The schematic shown in Figure 3.1 shows the decay stage from a compound nucleus. Proton evaporation is favoured in neutron-deficient nuclei over neutron evaporation as protons are more loosely bound than neutrons. The evaporated protons have a separation energy in the order of 2 MeV, and the order of $1\hbar$ of angular momentum. As evaporated neutrons have a greater separation energy for neutron-deficient nuclei, different reaction channels will be produced resulting in different spins occurring.

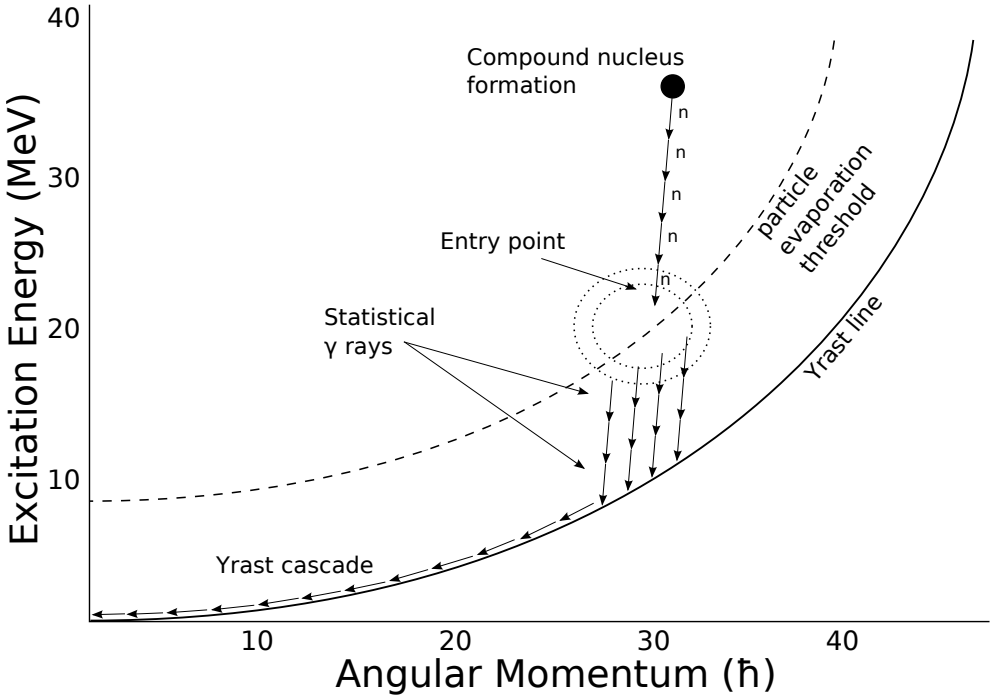

Figure 3.1: This schematic shows a five particle channel of a fusion-evaporation reaction, i.e. five nucleons. Once the particle-evaporation threshold is reached, then energy and angular momentum are lost as statistical γ-rays.

It is also possible for particle emission to occur as spontaneous radioactive decay modes from yrast states [20]. This is highly sensitive to the interplay of decay Q values and the orbital angular momenta of the emitting states.

3.2 Advances in Spectroscopy

In fusion-evaporation reactions, several reaction channels occur. This can be useful as it means many different nuclei can be populated in one experiment. However this introduces a large γ-ray background that could obscure the reaction channel of interest. Competing reaction channels is not the only source of the background, as Coulomb excitation of the target by the beam is also a factor.

Due to the large background obscuring the potentially weak electromagnetic transitions, a recoil separator combined with detectors at the focal plane allows the use of selective tagging techniques. The recoil separator allows fission products and unreacted beam to be separated from the recoiling residual nuclei which travel to the focal plane.

Data from every detector channel are recorded with an associated time stamp from a 10 ns metronome brought about by a 100 MHz hardware clock to allow for event reconstruction during analysis. The timestamps allow temporal correlations between γ rays emitted at the target position and recoil implantations and their subsequent decays detected at the focal plane of the recoil separator. This technique is called Recoil-Decay Tagging (RDT) [3, 21].

3.3 Experimental Apparatus

The University of Jyväskylä Accelerator Laboratory utilises a K130 cyclotron to provide a beam selected with a specific target to produce the required compound nucleus for the experiment. The charged particle and electromagnetic emissions are observed by the Lisa spectrometer, the Jurogam II spectrometer [22], and the Great spectrometer [23]. Figure 3.2 shows the beam line coming into the photograph from the right hand side, with the Jurogam II spectrometer centre-left.

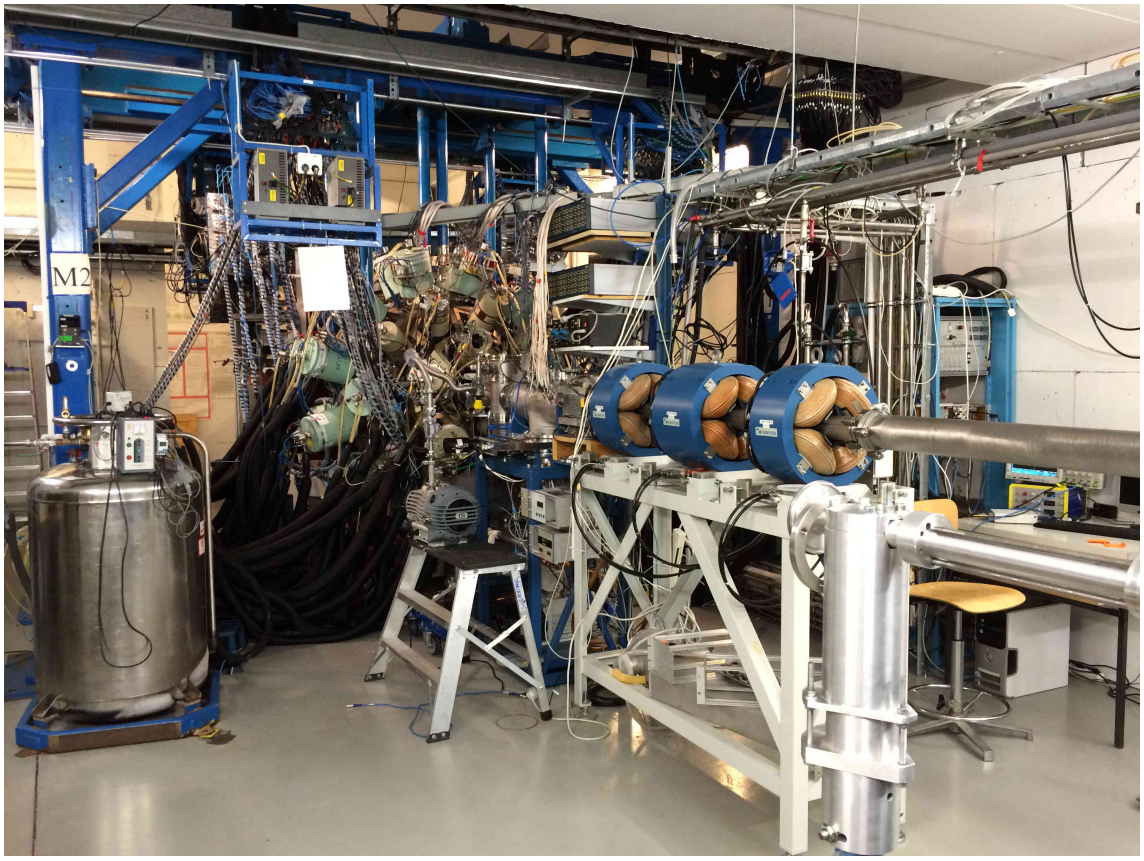

Figure 3.2: The JUROGAM II γ-ray spectrometer located at the RITU target position. The beam direction is from right to left.

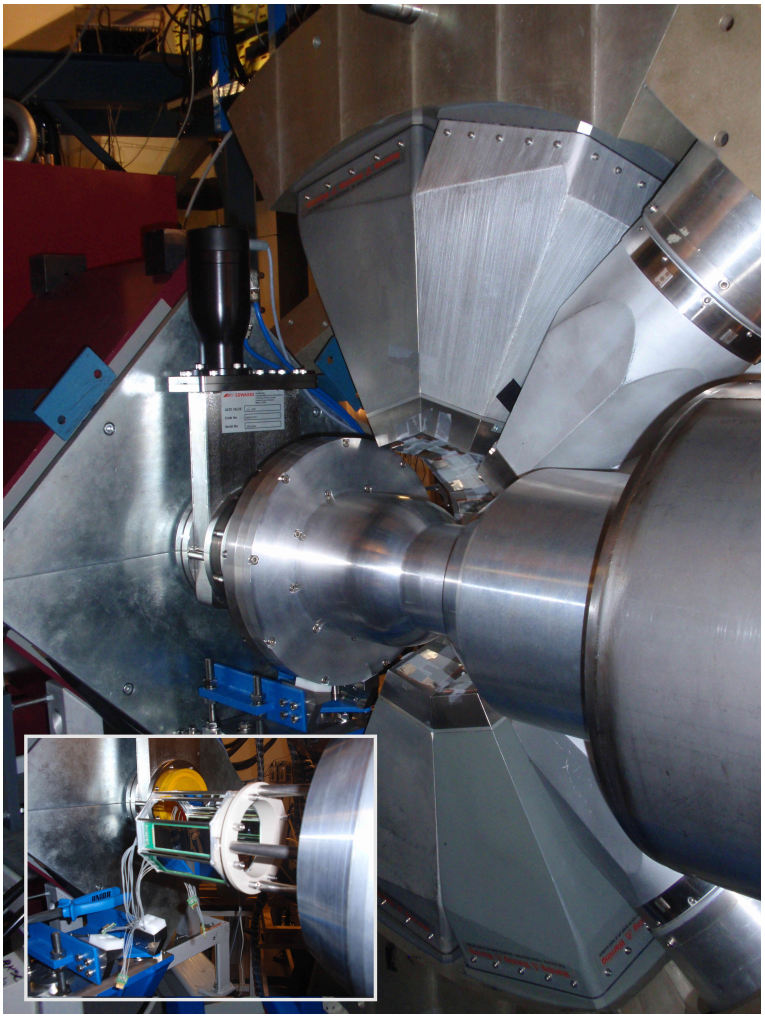

Figure 3.3: The LISA light-ion spectrometer array installed inside JUROGAM II at the target position [24].

3.3.1 The LISA Spectrometer

The Light Ion Spectrometer Array (LISA) see Figure 3.3 [24] is used in conjunction with the JUROGAM II and GREAT spectrometers.

The LISA spectrometer can distinguish between evaporated proton and α particles since the spectrometer comprises $\delta E - E$ telescopes. However, for this experiment there was only a partial implementation with a single layer of silicon and this discrimination was not possible. Instead we have used the raw fold of evaporated particles as can be seen later in Chapter 4.

LISA can be used in combination with RDT to measure nuclei on the proton-drip line with extremely short lifetimes, in the order of 0.5 μs and less. An array of silicon detectors placed in different orientations make up the LISA spectrometer, and it is designed to be placed at the target position in the RITU-γ cave in Jyväskylä. The spectrometer allows the measurement of charged particles, and is used with JUROGAM II detecting γ rays.

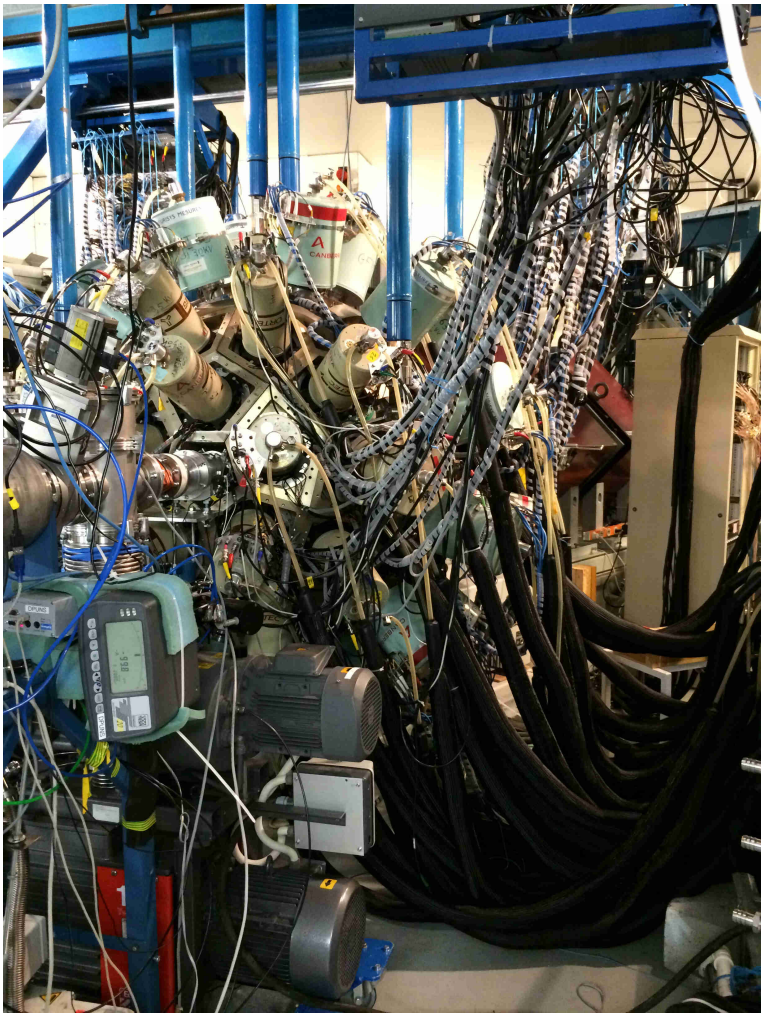

Figure 3.4: The JUROGAM II array at the target position with data cables above and autofill tubes below. The smaller cryostats are attached to the Phase 1 detectors, whereas the larger cryostats are Clover detectors.

3.3.2 The JUROGAM II Spectrometer

JUROGAM II is a High-Purity Germanium (HPGe) detector array (shown in the photograph in Figure 3.4) consisting of 24 Clover detectors [25] and 15 Phase 1 detectors [26]. In this experiment, 5 Phase 1 detectors were removed to allow LISA to be fitted. Clover detectors have 4 segmented germanium crystals and Phase 1 detectors, named as such as they were present before the JUROGAM II upgrade, have a single germanium crystal; as can be seen schematically in Figure 3.5.

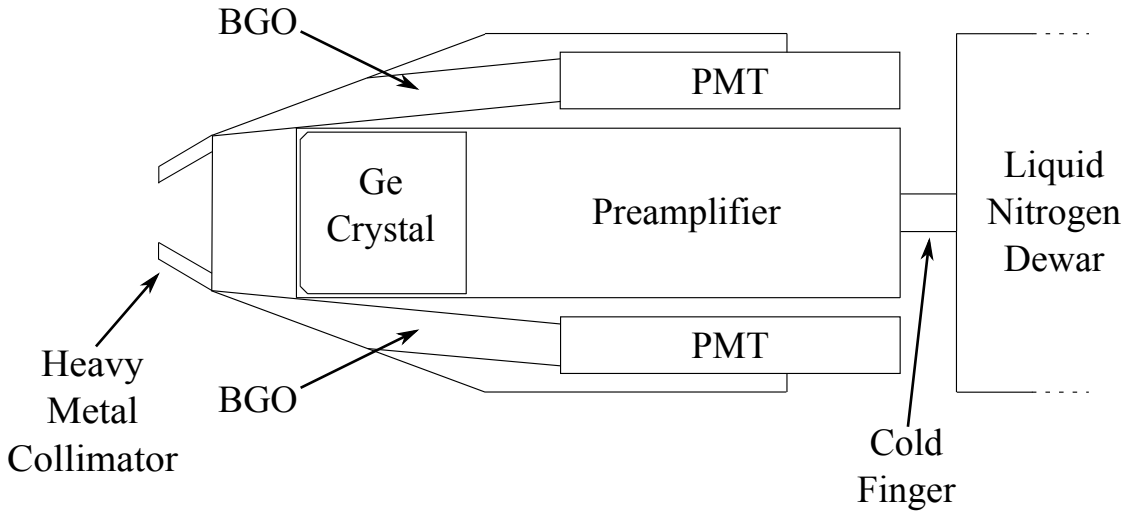

Figure 3.5: This is a schematic representation of a Phase 1 HPGe detector. The HPGe crystal and preamplifier are enclosed inside a vacuum in which a cold finger connects between the crystal and an external liquid nitrogen dewar. This is then placed inside a BGO shield that is held in place by the JUROGAM II frame. This diagram is not to scale [26].

HPGe semiconductor detectors are used in high-resolution γ-ray spectroscopy to identify discrete γ-ray energies. HPGe detectors must be cooled with liquid nitrogen via a cold finger to reduce noise caused by thermal excitations across the energy gap, as shown in Figure 3.5.

The HPGe detectors are mounted in a frame that contains a bismuth germanate scintillator shield (BGO) which is used as a Compton-escape suppression shield. Signals in the HPGe detectors that are in coincidence with signals in the BGO shield are discarded as they represent γ rays that have Compton scattered out of the detectors and therefore have not deposited their full energy inside the detector.

Table 3.1: The angles of detectors in the JUROGAM II array. (a) T is a tapered Phase 1 coaxial detector, Q is a Clover detector. All angles are defined with respect to the beam direction. All angles are midpoint angles. Each Clover detector has four crystals - a, b, c, d arranged in a clockwise fashion when viewed from the Dewar side of the detector. The detectors are mounted such that the c and d crystals are closest to $\theta = 90°$. Each of the four crystal's midpoint angles subtend 4.5°. [27]

Array Position [(a)]	$\theta°$
T06 to T15	133.57
Q01 to Q12	104.5
Q13 to Q24	75.5

Heavy metal collimators shield the BGO detectors to reduce discarded counts in the HPGe detectors from mis-matched Compton-escaped events due to γ rays entering the BGO shields directly. The detector angles in the JUROGAM II array are shown in Table 3.1 [27].

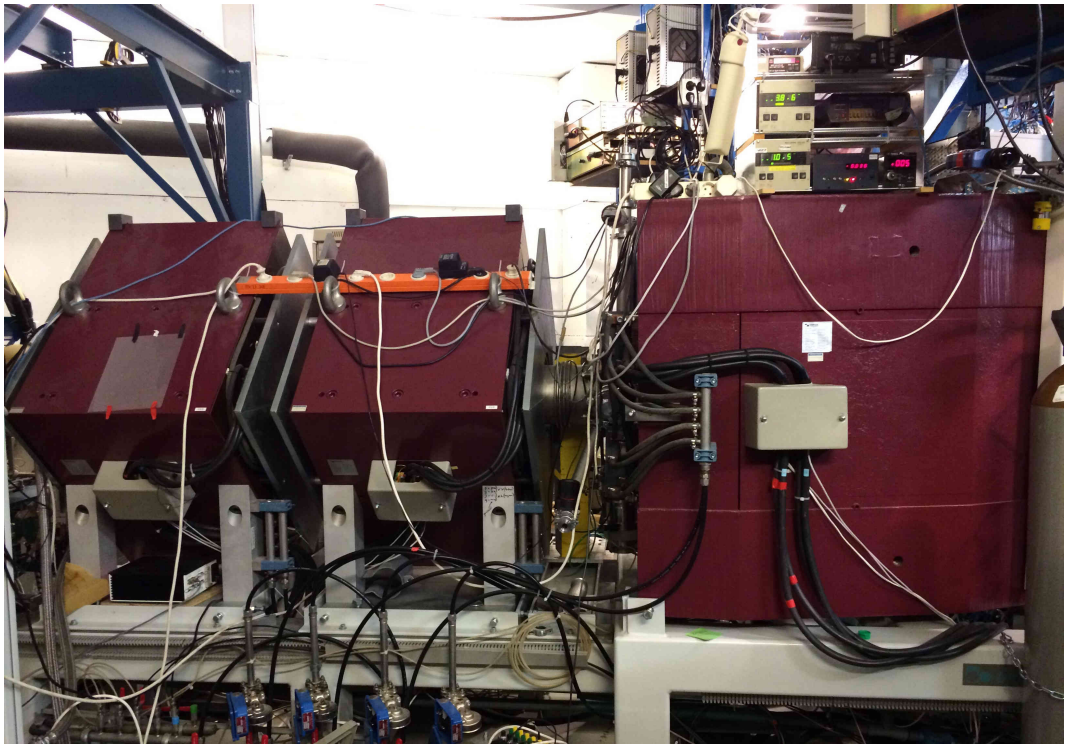

Figure 3.6: The RITU gas-filled separator. The beam direction is from right to left.

3.3.3 The RITU gas filled separator

The Recoil Ion Transfer Unit (RITU) [28, 29, 30] is a gas-filled separator that separates the recoiling nuclei made in the fusion-evaporation reaction from unreacted beam and fission fragments, and subsequently transports the recoils to the GREAT spectrometer located at the focal plane, see Figure 3.6.

Recoils exit the target in a narrow forward-focused cone. The first quadrupole magnet at the entrance of RITU matches the fusion recoil cone to the acceptance of the dipole magnet. The dipole magnet then steers the recoils and dumps most of the unreacted beam into a Ta ski inside RITU. The separation between the recoiling nuclei and unreacted beam is dependant on the differences in the magnetic rigidities of the beam and fusion evaporation residues.

$$B\rho = \frac{m\nu}{eq}, \tag{3.6}$$

which determines the deflection of a particle in a magnetic field. After that a further two quadrupole magnets focus the recoils onto the GREAT spectrometer at the focal plane.

RITU is filled with helium gas. Recoiling fusion products and unreacted beam undergo charge exchange collisions in the gas, which results in them being transmitted to the focal plane detector in an average charge state. This results in a higher transmission efficiency over vacuum-mode separators which can only accept a few charge states at the expense of retaining any mass selectivity.

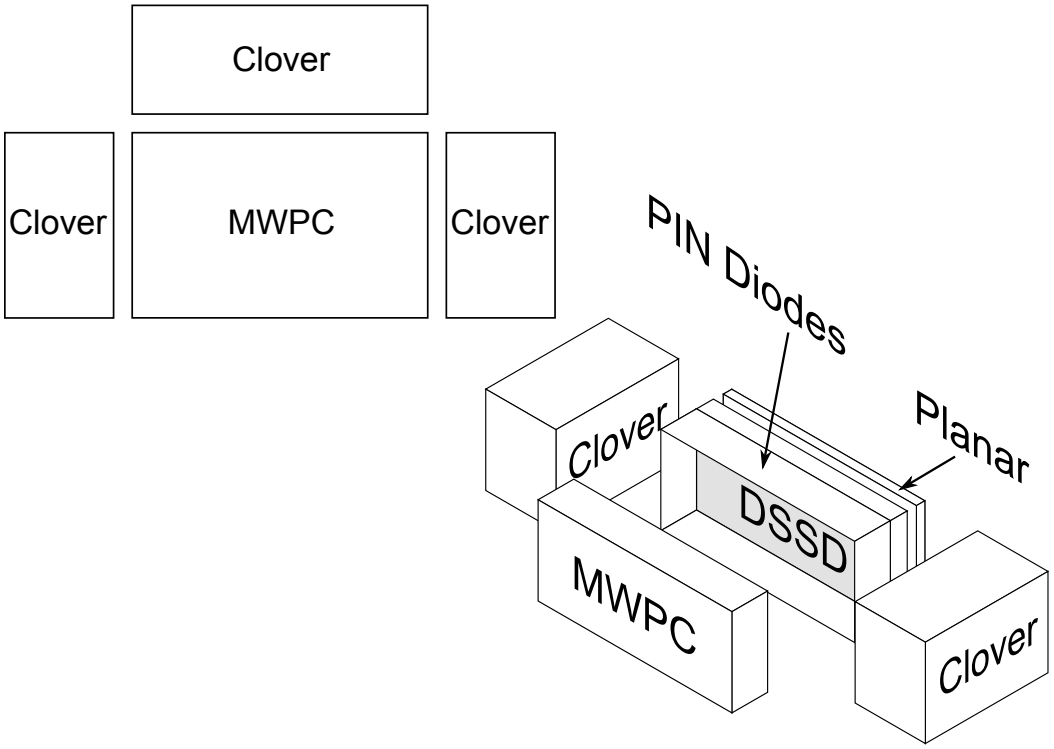

Figure 3.7: The GREAT spectrometer. Recoils from fusion-evaporation travel through the MWPC and are implanted into the DSSD array. Radiations from the recoil are detected by the DSSDs, PINs, Planar and Clover detectors. The large top Clover detector would be located vertically above the DSSD.

3.3.4 The GREAT spectrometer

The Gamma Recoil Electron Alpha Tagging (GREAT) spectrometer sits at the focal plane after RITU and is used to detect recoil implantations and their subsequent decays. Figure 3.7 shows a schematic diagram and a photograph is shown in Figure 3.8. It is made up of several different devices used to detect different radioactive decay modes of the arriving recoil nuclei.

Figure 3.9 shows a simplified version of a recoiling nucleus entering and interacting with the GREAT spectrometer. The recoiling nucleus passes through the Multi-Wire Proportional Counter (MWPC) and deposits energy with a time-of-flight component recorded by the Total Data Readout (TDR) system. The 'recoil' then passes through the PIN diodes array and is deposited into the Double-sided Sil-

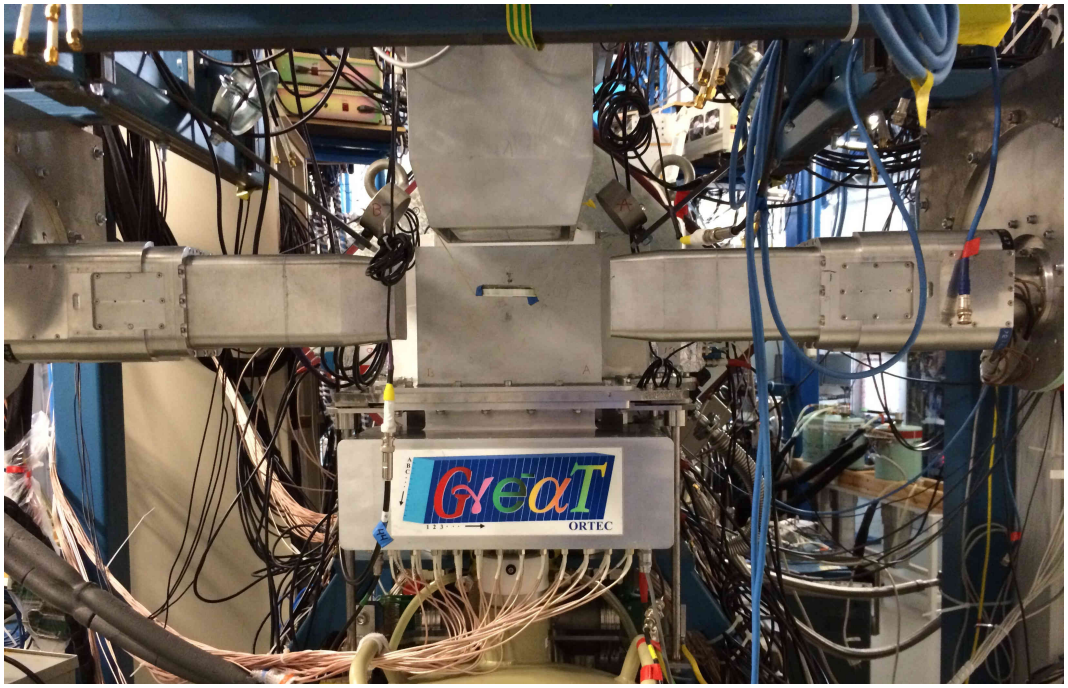

Figure 3.8: A view of GREAT at the focal plane looking upstream.

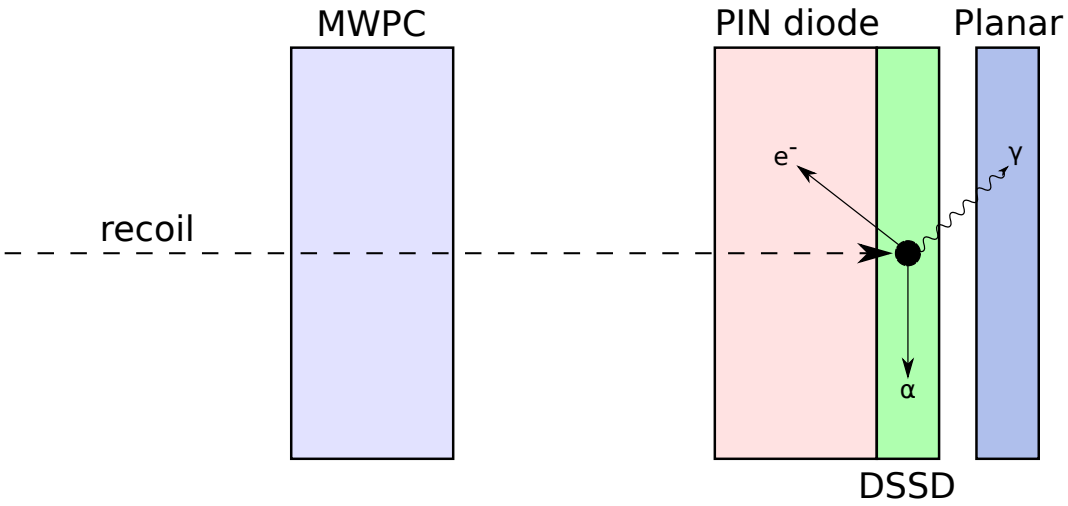

Figure 3.9: A side view of a recoil interacting with GREAT.

icon Strip Detector (DSSD) where it decays. The radioactive decays and conversion electrons are measured in the DSSD and PIN diode array, while the isomer-delayed γ-ray emissions are detected in the Planar and Clover Ge detectors.

Multi-Wire Proportional Counter (MWPC)

The Multi-Wire Proportional Counter (MWPC) is an isobutane filled detector positioned at the end of RITU and the start of the vacuum of GREAT separated by Mylar windows. As recoils pass through the MWPC, the isobutane is ionised and this charge is collected by the anodes allowing energy and time information to be collected. The detector can be used to discriminate between recoils and scattered beam.

Double-sided Silicon Strip Detector (DSSD)

These implantation detectors are a pair of adjacent 60 mm $\times$ 40 mm silicon detectors that are 300 μm thick and separated by 4 mm. Each DSSD has 60 $\times$ 40 strips resulting in a total of 4800 pixels which allows a high degree of spatial correlations due to accurate positioning of implantations. The DSSDs are enclosed and in close proximity to the preamplifiers so heat is generated which would cause thermal noise. To mitigate this problem detectors are mounted on cooling blocks and connected to an ethanol heat exchanger.

PIN diodes array

The 28 silicon detectors that make up the PIN diodes array are positioned in a shoebox arrangement between the MWPC and the DSSDs. The PINs can detect conversion electrons, β particles α particles that have escaped the DSSDs. For the set up of this experiment, the PINs were set up to detect escaped α particles. In this case most of the energy of the α particles detected will be spread out between the DSSDs and the PINs, so with the addition of the two energies detected, a reasonably accurate energy can be determined, but loss of energy between the detectors will cause accuracy limitations.

Planar Germanium Strip Detector

The planar is a double-sided detector, with the dimensions 60 mm × 40 mm and a total of 288 pixels, collects signals read from horizontal and vertical strips on the front and back of the detector. The planar detector is positioned 10 mm downstream of the DSSDs within the vacuum of GREAT and can detect X rays, low-energy γ rays and high-energy β particles. The front face of the planar is more appropriate for detecting X rays and γ rays with energies less than 100 keV as low-energy transitions may not penetrate far enough into the germanium. A beryllium entrance window of 0.5 mm separates the detector from the rest of the GREAT vacuum.

Focal Plane HPGe Clover Detector

The focal plane clover detector comprises of 4 coaxial n-type clover detectors, each of which has four-fold segmentation resulting in a detector with 16 active regions within one cryostat. The clover detector is used in conjunction with a BGO Compton-suppression shield and placed above the GREAT chamber. The geometry of the detector was designed to match the focal plane dimensions. Additional clover detectors may be added to face the sides of the GREAT chamber.

3.3.5 Total Data Readout (TDR)

Total Data Readout (TDR) is a triggerless data acquisition system [3, 21]. The TDR incorporates a 100 MHz metronome that timestamps every single detector signal with a 10 ns tick time. This reduces common dead time and allows higher data rate experiments to be run. A software trigger is then used to reconstruct events so that no data are lost. This also means that long correlation times can be used without losing any events. This is key to the processes required by RDT. A disadvantage of this method is that large amounts of data are produced for storage,

so a pre-filter can be used that accept events only if they follow certain conditions. For this experiment the pre-filter was set to only store data that can be correlated to events seen in the DSSDs.

3.4 Experimental Methodology

3.4.1 Calibrations

Before analysis is started a calibration of all the detectors must be carried out. Each detector has a unique calibration as the electronic gain on all detectors differ due to differences in hardware such as signal cable lengths. Radiation sources with known peak energies are placed inside each section of the experimental apparatus with the type of radiation specifically chosen for that detector system. ^{152}Eu and ^{133}Ba are used in JUROGAM II and are placed at the centre of the array, ^{239}Pu, ^{241}Am and ^{244}Cm are placed inside the focal plane for the calibration of the DSSDs and PINs. A mixed EuBa source is placed externally on GREAT to calibrate the planar and clover detectors at the focal plane.

For calibrating the HPGe detectors and planar detector, around 10 peaks are chosen across a range of 80 and 1408 keV and energy calibrated as a function of channel number using the equation

$$E = a + (channel\ no. \times b) + (channel\ no.^2 \times c) \tag{3.7}$$

where E is the energy, a, b and c are the quadratic term coefficients.

3.4.2 Doppler-shift correction

Although the target is at rest at the centre of JUROGAM II the beam impinged upon it is not. The reaction products from fusion-evaporation are thrown forward from the target position. The γ rays that are emitted in the forward direction ($0^o \leq \theta < 90^o$ relative to the beam axis) from the moving nuclei experience an increase in energy, whereas those emitted in the backward direction ($90^o < \theta \leq 180^o$) will experience a decrease in energy.

The Doppler-shift correction [31] must be applied to γ rays detected in JUROGAM II to account for these energy shifts at different angles,

$$E = E_0 \left(1 + \frac{v}{c} cos\left(\theta\right)\right) \tag{3.8}$$

where E is the detected energy, E_0 is the true energy, $\frac{v}{c}$ is the nucleus velocity, and θ is the angle of the detector relative to the beam axis. The $\frac{v}{c}$ parameter is the unknown in this equation and can be measured by observing differences in detected peak energies in detectors at different angles in JUROGAM II.

3.4.3 Efficiency Correction

Knowing the relative intensities of the detected γ rays is essential information for several parts of the analysis. Just as the energies of the peaks need to be calibrated, so do the peak intensities. The JUROGAM II array is most efficient at around 120 keV due to the size of the crystal and how γ-ray energies are absorbed by the detectors and surrounding objects (such as the target chamber which attenuates lower energy γ rays). For efficiency calibrations the ^{152}Eu and ^{133}Ba sources used also for the energy calibration are placed at the target position and the JUROGAM II array is closed to simulate the conditions found in an experiment (one difference being, the calibration sources are at rest). Figure 3.10 displays the efficiency curve of JUROGAM II in this particular setup.

3.5 Experimental Techniques

The following range of techniques are used to allow information on the desired nucleus to be extracted from the data collected by the equipment described in the previous section.

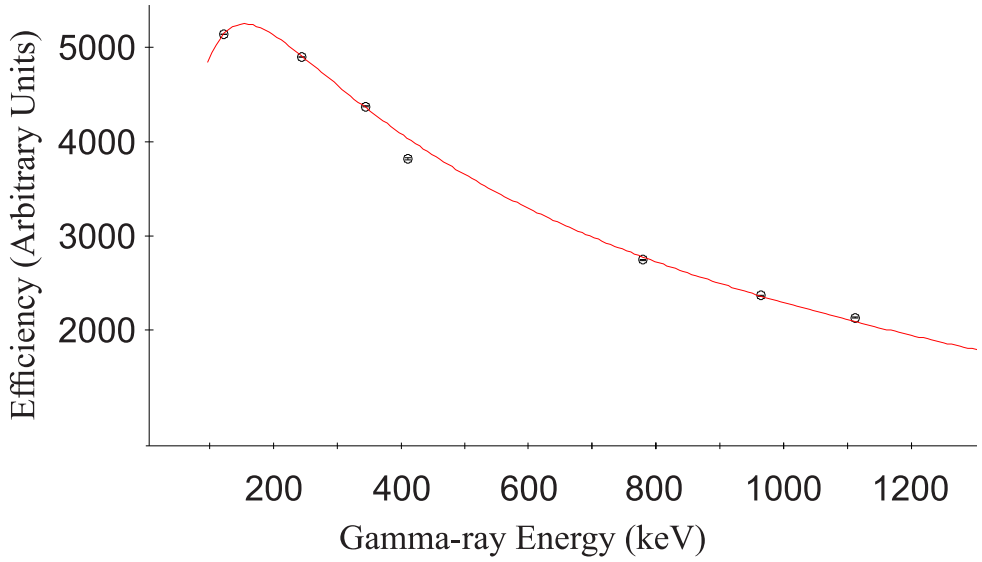

Figure 3.10: The efficiency curve of JUROGAM II produced using the analysis software package Radware [32].

3.5.1 Tagging Techniques

There are many reaction channels available in the data from the fusion-evaporation reaction. Selection of a specific channel is often essential for the analysis of a certain nucleus particularly for γ-ray emissions in nuclei produced with low cross sections in a large γ-ray background arising from other reaction channels to reduce the large γ-ray background.

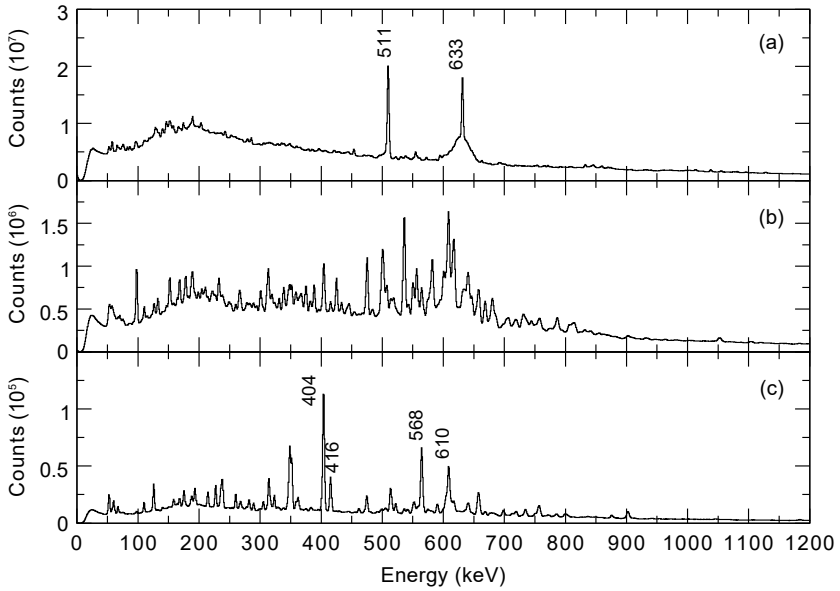

Figure 3.11: Spectrum (a) shows raw JUROGAM II untagged data. The only obvious peaks are the 511 keV peak and Coulomb excitation peak at 633 keV from the ^{106}Cd target. Spectrum (b) shows the recoil-decay tagged ^{158}Lu with only an energy gate on the 76 keV and 170 keV peaks in the focal plane. Spectrum (c) is the isomer recoil decay tagged spectrum with an additional gate to the panel above around the half-life of the isomeric state in ^{158}Lu discussed in (Chapter 4).

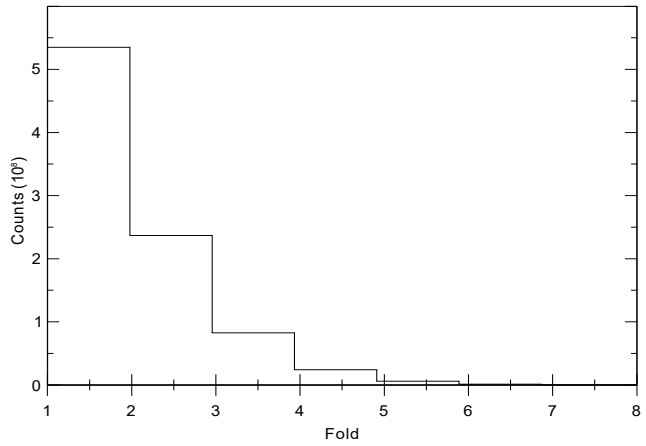

Figure 3.12: This shows the JUROGAM II fold with obtained for γ rays detected in delayed coincidence with a recoil implantation at the RITU focal plane.

In Figure 3.11 the top spectrum shows a JUROGAM II untagged spectrum which demonstrates how important tagging techniques are in order to extract meaningful information from spectra obtained from a complex reaction. There is a high level of background and the large, wide peak around 600 keV is caused by Coulomb Excitation of the beam (a "Coulex Peak") which hides useful information. This can be eliminated by setting a γ-γ time gate to ensure only coincidences are accepted. The middle spectrum is recoil-gated JUROGAM II meaning recoiling particles of a certain energy can be selected in the DSSD and correlated with specific γ rays originating from a particular reaction channels compound nucleus. The bottom spectrum is isomer recoil-gated JUROGAM II which incorporates an additional lifetime component and using delayed γ rays detected by HPGe Clover detectors in the focal plane.

The JUROGAM II fold for RDT and Isomer RDT can be seen in Figures 3.12 and 3.13 which demonstrates the reduction of statistics between the two techniques as indicated by the fold distributions. Note that the fold distribution also has a reaction and angular momentum dependence.

Figure 3.14 is a two-dimensional matrix displaying energy versus time-of-flight

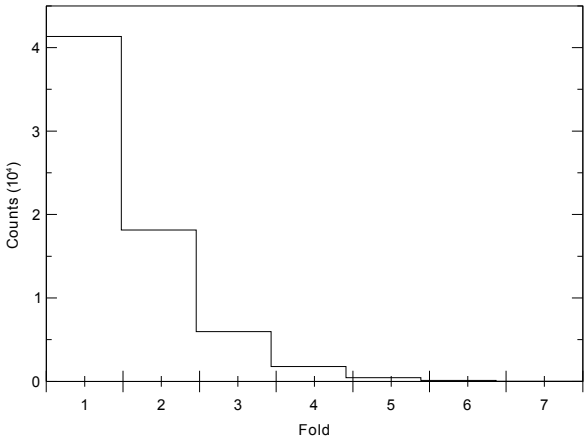

Figure 3.13: This shows the JUROGAM II fold obtained from prompt γ rays detected in delayed coincidence with γ rays de-exciting isomeric states at the RITU focal plane.

of recoils between the MWPC and DSSD in the GREAT spectrometer. The dashed line represents a two-dimensional energy gate that is placed around the recoiling nuclei and makes up the energy selection component (known as a 'gate') of the recoil tagging for RDT in the sort code.

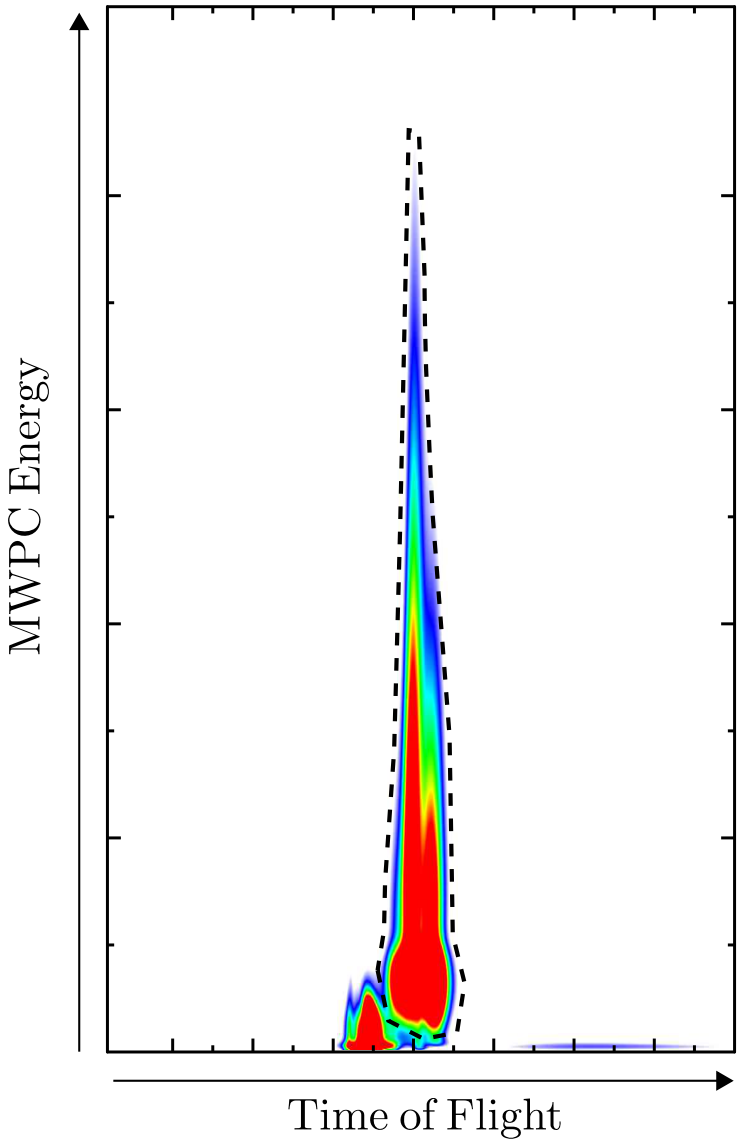

Figure 3.14: Energy deposited by recoiling nuclei and scattered beam in the MWPC versus the flight time between the MWPC and the DSSD. The reaction used here is a ^{58}Ni beam with a ^{106}Cd target at a beam energy of 318 MeV. The larger component, highlighted with a dashed line, is a two-dimensional gate selecting the recoiling nuclei. The smaller component to the left is unreacted scattered beam.

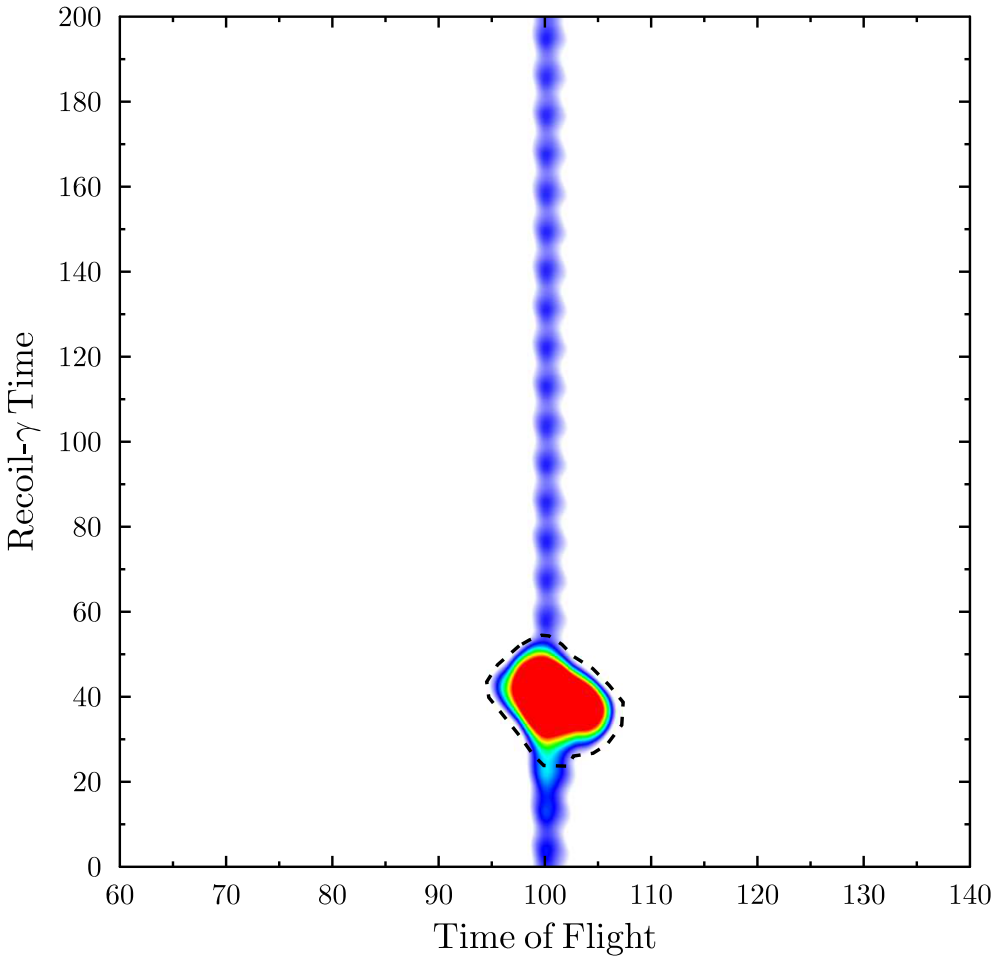

Figure 3.15: Recoil-γ time in JUROGAM II versus the flight time between the MWPC and the DSSD. The larger component, highlighted with a dashed line, is a two-dimensional time gate selecting the time component of the recoiling nuclei for RDT. The smaller peaks above and below originate from the cyclotron beam's oscillation frequency, commonly referred to as 'cyclotron bumps'.

Figure 3.15 is a two-dimensional matrix displaying time versus time-of-flight of recoils between the MWPC and DSSD in the GREAT spectrometer. As with the two-dimensional gate in Figure 3.14, here the gate is around the time component of the recoil tagging for RDT.

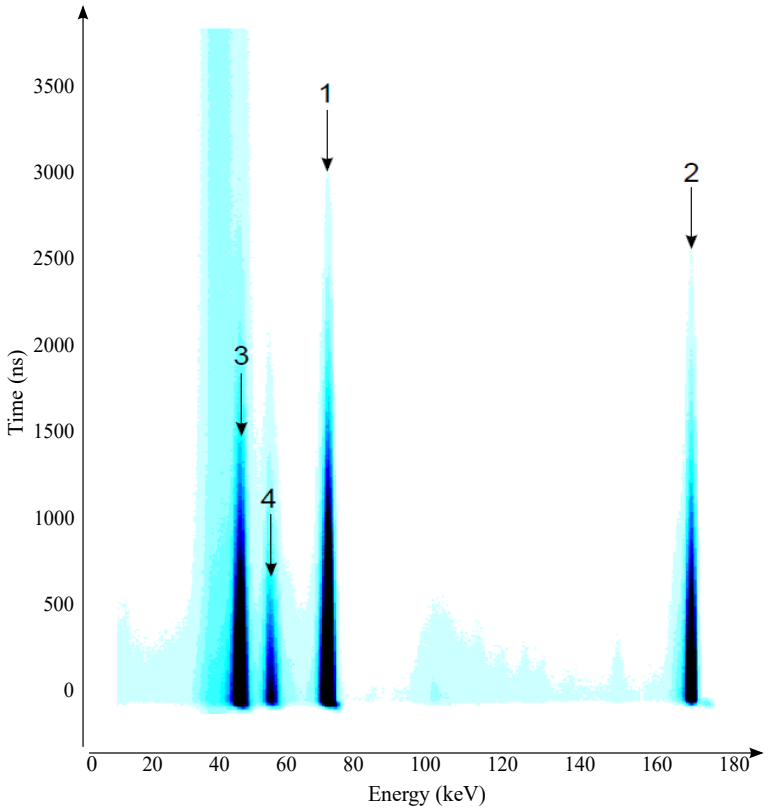

Figure 3.16: A plot of time differences between the detection of a recoil implantation in the GREAT DSSD and the detection of γ-ray transitions in the planar detector. Peaks 1 and 2 correspond to the 76 keV and 170 keV γ rays depopulating the isomeric state in ^{158}Lu. The lower energy peaks 3 and 4 are X-ray transitions.

Figure 3.16 shows a two-dimensional matrix displaying focal plane clover time versus energy in the GREAT spectrometer. This is produced to determine isomeric decay lifetimes of different γ-ray peaks in the focal plane, which is set up to measure delayed γ rays, therefore detecting isomeric states in the ns to μs time regime. Using the analysis software GRAIN [33] to produce a slice of this matrix allows one to 'gate' on a γ ray, set a background subtraction, and to view a background subtracted lifetime curve, as shown in Section 4.

Chapter 4

Spectroscopy of the exotic nuclei ^{156}Lu and ^{158}Lu

Excited states of the neutron-deficient nuclei ^{156}Lu and ^{158}Lu have been populated with the fusion-evaporation reactions ^{106}Cd(^{58}Ni, α3pn) and ^{106}Cd(^{58}Ni, 5pn), respectively. The experiment was performed at the University of Jyväskylä Accelerator Laboratory (JYFL) where prompt γ rays were detected at the target position of the JUROGAM II array. The JUROGAM II spectrometer array was coupled to the RITU separator, which transported recoiling fusion evaporation residues to the GREAT spectrometer at the focal plane. Isomeric states have been discovered, and their lifetimes measured, in both nuclides. A large number of new γ-ray transitions have been observed in ^{156}Lu with amendments to previous work on this nucleus and a level scheme has been established for the low-spin states in ^{158}Lu for the first time.

4.1 Previous work

The isotope ^{156}Lu was first identified by the observation of its characteristic α emissions. Hofmann *et al.* [34] discovered two α decays with E_α = 5.450(10) MeV; $t_{1/2}$ = 500 ms, and E_α = 5.567(5) MeV; $t_{1/2}$ = 180(20) ms with b_α = 100(25)% [34]. Further work was done by Page *et al.* who made high precision measurements as part of a wider study of neutron-deficient isotopes in the $N > 82 > Z$ region [35]. Page *et al.* obtained values of E_α = 5.454(4) MeV; $t_{1/2}$ = 494(12) ms, and E_α = 5.565(4) MeV; $t_{1/2}$ = 198(2) ms with b_α = 98(9)% [35].

A level scheme of excited states in ^{156}Lu was established by Ding *et al.* [4] (see Figure 1.2 in Chapter 1). Ding *et al.* used the characteristic α decays measured in the previous studies in a mass-selected recoil-decay tagging experiment. This experiment used the GAMMASPHERE spectrometer array comprising 101 Germanium detectors coupled to the Fragment Mass Analyzer. The recoil-decay tagging was achieved by recording the recoils of 25^+ and 26^+ charge states of A = 156 recoils collected at the separator focal plane. Recoil-decay correlations were limited to 200 ms. Ding *et al.* [4] produced a significant level scheme extending to high excitation energy. The level scheme has been amended in this thesis and new excited states including an isomer have been discovered.

The isotope ^{158}Lu was discovered in 1980 by Alkhazov *et al.* by its α decay [36]. The nucleus was investigated using the IRIS online mass separator facility at LINP (Gatchina, USSR). A spallation reaction induced by bombarding a 1 GeV proton beam onto a tungsten target produced the ^{158}Lu. Alkhazov *et al.* measured the α-decay energy to be 4.665(10) MeV with a half-life of 10(1) s [36]. Toth *et al.* used the ^{144}Sm(^{19}F, 5n)^{158}Lu and ^{144}Sm(^{19}F, 8n)^{158}Lu reactions to measure the α-decay properties of ^{158}Lu and obtain cross-bombardment information [37]. The helium gas-jet technique was used to collect and transport reaction products [37] so that

they could be assayed for radioactivity with surface barrier Si (Au) detectors. In this experiment, Toth measured a consistent value for the α-decay energy 4.666(5) MeV and determined the half-life to be 9(2) s [37].

The excited states in ^{158}Lu were first investigated by Dracoulis *et al.* in experiments using the CAESAR γ-ray spectrometer at the Australian National University and the HERA spectrometer at the Lawrence Berkeley National Laboratory [38]. A γ-ray spectrum was shown in conference proceedings, however no level scheme was published for ^{158}Lu in that work or elsewhere in the literature. The current work confirms the γ rays observed by Dracoulis *et al.* and establishes the first level scheme for this nucleus.

4.2 Experimental Details

The fusion-evaporation reactions ^{58}Ni(^{106}Cd, α3pn) and ^{58}Ni(^{106}Cd, 5pn) were used to populate excited states in the neutron-deficient nuclides ^{156}Lu and ^{158}Lu, respectively. The K130 cyclotron at the University of Jyväskylä Accelerator Laboratory accelerated the ^{58}Ni ions to an energy of 318 MeV with an average beam intensity of 7 pnA focused onto the target. The ^{106}Cd target was enriched to the 96% level and had a nominal thickness of 975 μg/cm^2. Table 4.1 lists calculated estimates for the relative population of the exit channels following the ^{58}Ni + ^{106}Cd reaction at a bombarding energy of 318 MeV using the PACE4 fusion evaporation code [39]. The Lu isotopes are predicted to be populated at reasonable cross sections for γ-ray spectroscopy studies.

The target was placed in the centre of the JUROGAM II array. The JUROGAM II array comprised 10 EUROGAM-type HPGe detectors at an angle of 133.57°, 12 Clover HPGe detectors at an angle of 104.5° and 12 Clover HPGe detectors at an angle of 75.5° relative to the beam direction. The target was surrounded by the

Table 4.1: A Projection Angular-momentum Coupled Evaporation (PACE4) Monte Carlo code calculation estimating the relative population of the channels following the ^{58}Ni + ^{106}Cd reaction at a bombarding energy of 318 MeV. The nuclides ^{156}Lu and ^{158}Lu are indicated by bold type.

Nuclide	Cross Section (mb)
^{159}Ta	19
^{159}Hf	28
^{158}Ta	3
^{158}Hf	33
^{158}**Lu**	**13**
^{156}**Lu**	**38**
^{156}Yb	22
^{156}Hf	66
^{155}Lu	19
^{155}Yb	32
^{153}Lu	18
^{153}Yb	62
^{152}Yb	44
^{152}Tm	35
^{150}Er	70

LISA light-ion Si spectrometer array.

Recoiling fusion-evaporation products were separated in-flight from fission products and primary beam by the RITU gas-filled separator and transported to the GREAT spectrometer, which is located at the focal plane. Genuine recoils were distinguished from scattered beam by energy loss in the GREAT MWPC and, in conjunction with the DSSD, time-of-flight measurements [40, 41]. The total data readout (TDR) [3] data acquisition system timestamped all detected signals individually to a precision of 10 ns. The data were sorted both online and offline with the GRAIN [33] software package. Offline γ-ray coincidence analysis was performed in the Radware [32] software package.

4.3 Results: ^{156}Lu

4.3.1 Recoil-decay correlations in ^{156}Lu

The two previously reported α-decaying states in ^{156}Lu [42, 34, 4] are assigned the spins and parities (2^-) and (9^+) and their α-decay properties are listed in Table 4.2. Figure 4.1(a) shows an α-decay spectrum from the present work. This spectrum shows α decays detected following a recoil implantation within the same DSSD pixel within 2 s. The $\alpha(^{156}$Lu)-decay peak is prominent in the spectrum, however, there are many other α decays in the spectrum arising from the large number of other fusion-evaporation products and their subsequent decays. Figure 4.1(b) expands the spectrum around the α-decay from the 9^+ state. There is some overlap with the α-decay peak originating from ^{158}Ta. Thus recoil-$\alpha(^{156}$Lu)-correlated γ-ray spectra have the potential to be contaminated by γ rays arising from recoil-α-decay correlations with ^{158}Ta due to their overlapping peaks and their similar α-decay half-lives.

Figure 4.2(a) shows a spectrum of γ rays that have delayed coincidences with recoil implantations at the focal plane of the RITU separator. Previously reported γ-ray transitions originating from the reaction products are apparent in this spectrum. Figure 4.2(b) shows a γ-ray spectrum produced by demanding correlations that have the additional constraint of being followed by the subsequent 9^+ α decay of ^{156}Lu in the same DSSD pixel within 2 s. The recoil-decay correlations clearly bias the data towards the previously identified transitions of ^{156}Lu. The previous level scheme

Table 4.2: Alpha-decay properties of the ground state and low-lying isomer in ^{156}Lu.

Nucleus	E_α (keV)	$t_{1/2}$ (ms)	$J_i^\pi \rightarrow J_f^\pi$
$^{156}Lu_{(2^-)}$	5454(4)	494(12)	$(2^-) \rightarrow (2^-)$
$^{156}Lu_{(9^+)}$	5565(4)	198(2)	$(9^+) \rightarrow (9^+)$

for ^{156}Lu by Ding *et al.* [4], see Figure 1.2, was produced using mass-selected recoils with and without subsequent decay correlations using the 9^+ isomer and had a lower degree of contamination. However, while the RITU gas-filled separator does not have any mass selection capabilities, it has a transmission efficiency that is an order of magnitude higher than the Fragment Mass Analyser used by Ding *et al.*.

This results in a larger number of tagged-$\gamma\gamma$ coincidences, see Figure 4.2. The effects of contamination in the γ-ray coincidence analysis has been mitigated by the improved statistics and the existing knowledge of the most intense γ rays in ^{156}Lu and nearby nuclei. In this work, it has been possible to amend and extend the ^{156}Lu level scheme above the 9^+ isomer.

It has not been possible to deduce any γ-ray transitions feeding the 2^- state in ^{156}Lu. Figure 4.3(a) and (b) show γ-ray spectra selected by recoil decay correlations using the 5453 keV (2^-) and 5565 keV (9^+) α decays, respectively. The spectra are almost indistinguishable from each other. This is not surprising since fusion-evaporation reactions preferentially populate yrast states so, in this case, the yrast intensity is trapped at the α-decaying 9^+ state. Consequently the 5453 keV (2^-) α decay is less prominent in this data. Indeed, Figure 4.1(b) shows that the ground-state α decay is completely obscured by the background formed by escaping α particles from the 5565 keV (9^+) α peaks and other higher energy decays.

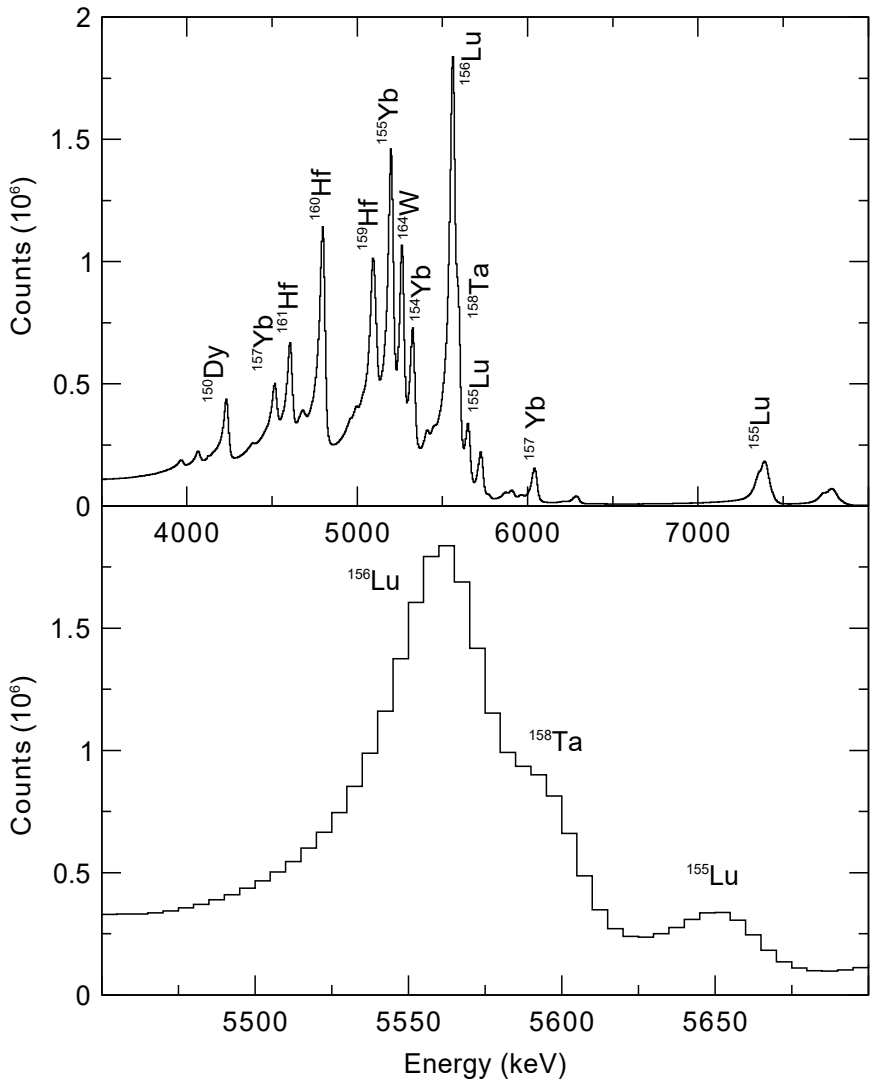

Figure 4.1: (a) Spectrum showing α decays detected following a recoil implantation within the same pixel within 2 s. The α decay from the 9^+ state in ^{156}Lu is the largest peak in the spectrum. (b) The region close to the ^{156}Lu originating from the α decay of the 9^+ isomer showing an overlapping α decay originating from ^{158}Ta. [2]

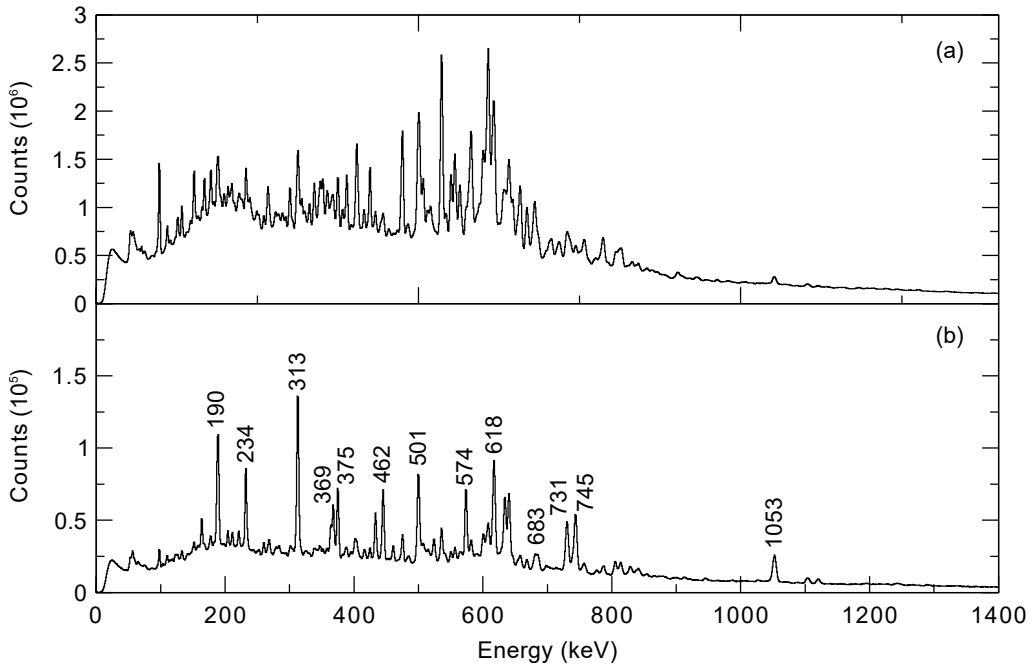

Figure 4.2: (a) γ-ray spectrum detected at the target position by JUROGAM II and correlated with a recoil implantation in the GREAT DSSD detectors at the focal plane. (b) γ-ray spectrum detected at the target position by JUROGAM II and correlated with recoil implantations followed by the characteristic 9^+ α decay of ^{156}Lu within the same DSSD pixel. The recoil-decay correlation time was limited to 2 seconds.

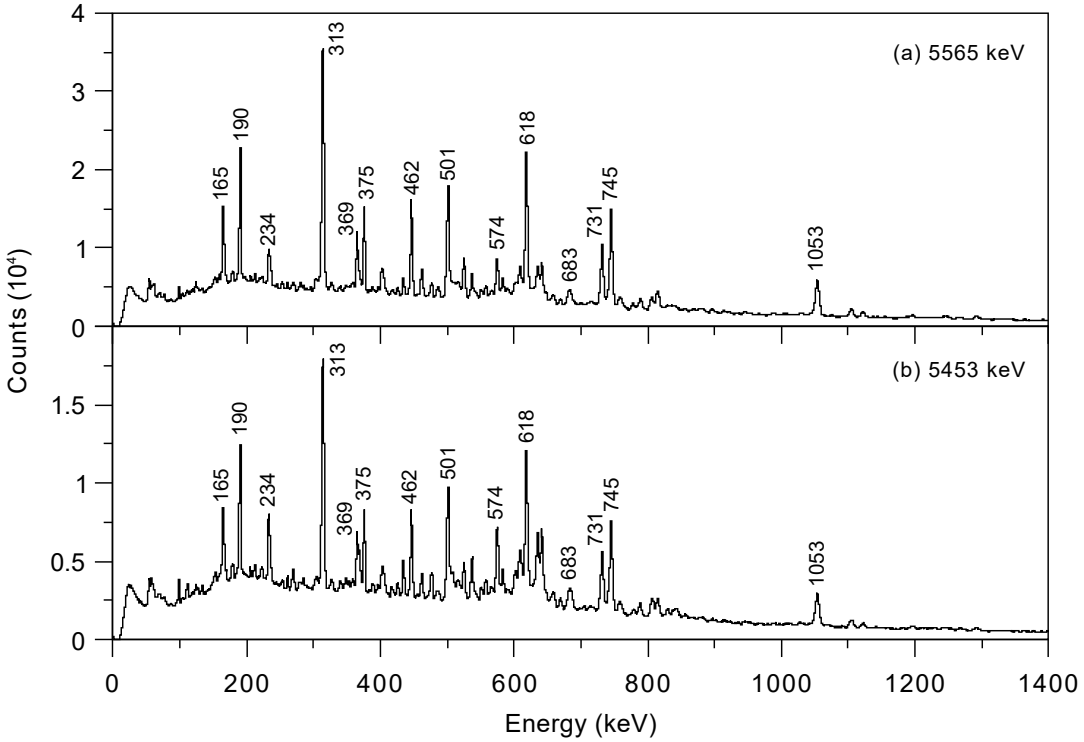

Figure 4.3: (a) Spectrum showing γ rays correlated with recoil implantations followed by the 5565 keV (9^+) α decay of ^{156}Lu within the same pixel. The correlation times were limited to 2 s, which corresponds to $\sim$10 half-lives. (b) Spectrum showing γ rays correlated with recoil implantations followed by the 5453 keV (2^-) α decay of ^{156}Lu within the same pixel. The correlation times were limited to 2 s, which corresponds to $\sim$4 half-lives for each decay.

4.3.2 JUROGAM II $\gamma\gamma$ coincidence analysis

γ-ray coincidences correlated with recoil implantations followed by an α decay from the 9^+ isomer within the same DSSD pixel were sorted offline into a $E_{\gamma 1} - E_{\gamma 2}$ matrix. This matrix was used to generate spectra to build the level scheme shown in Figure 4.4. It is noted that Ding *et al.* identified and assigned γ rays feeding the 10^+ state rather than the α-decaying 9^+ state. Figure 4.5 shows γ-ray coincidences between low-lying transitions in ^{156}Lu. Figures 4.5(a) and 4.5(b) show γ rays in coincidence with the 618 keV and 313 keV, transitions, respectively. These spectra show that these γ rays are in coincidence with the 745 keV transition assigned by Ding *et al.* to feed the low-lying 10^+ state. The spectra also show a weak 683 keV transition, which is not in coincidence with the 745 keV. Figure 4.5(c) shows that the 683 keV transition is in coincidence with the transitions between higher-lying excited states, which suggests it forms part of a parallel decay path from the 12^+ state. The 683 keV transition is assigned to feed directly the α-decaying 9^+ isomer. No linking transitions have been observed between the 618 keV and 683 keV γ rays suggesting that such transitions may have low energy and cannot be efficiently detected by the spectrometer array.

Figures 4.6 and 4.7 show typical γ-ray coincidence spectra extracted from the matrix that were used to significantly extend the level scheme for ^{156}Lu, see Figure 4.4. Figure 4.6(a) shows γ rays in coincidence with the 745 keV transition, which was identified as the lowest-lying transition feeding the 10^+ state by Ding *et al* [4]. Figure 4.6(b),(c) and (d) confirm that there are two parallel cascades that feed the low-spin states via the 574 keV transition. The 574 keV and 462 keV transitions had been observed by Ding *et al.* who assigned the latter transition to be a linking transition from an 18^+ state to the 16^+ state. Figures 4.6(c) shows γ rays in coincidence with the 462 keV transition, which indicates that it is part of a short cascade comprising the 123 keV, 313 keV, 487 keV and 574 keV transitions. The coincidences

with the 574 keV, see Figure 4.6(b), indicate several other intense transitions such as the 635 keV transition. Figure 4.6(d) shows γ rays in coincidence with the 635 keV transition and reveals γ rays in a cascade extending to high-spin and excitation energy. It is apparent from these spectra that the 574 keV transition forms a common link from two parallel structures to the previously assigned 16^+ state.

The transitions in the cascade observed by Ding *et al.* have been confirmed in this work but have been reordered on the basis of relative intensity measurements and to reflect the multiplet structure of the single-particle excitations. Figure 4.7(a) shows coincidences with the 1053 keV transition, which shows the transitions between low-spin states observed by Ding *et al.* and several new high-energy transitions notably 1105 keV, 1121 keV and 1242 keV transitions. Figure 4.7 indicates that these transitions form part of three distinct branches extending to higher spins and excitation energies.

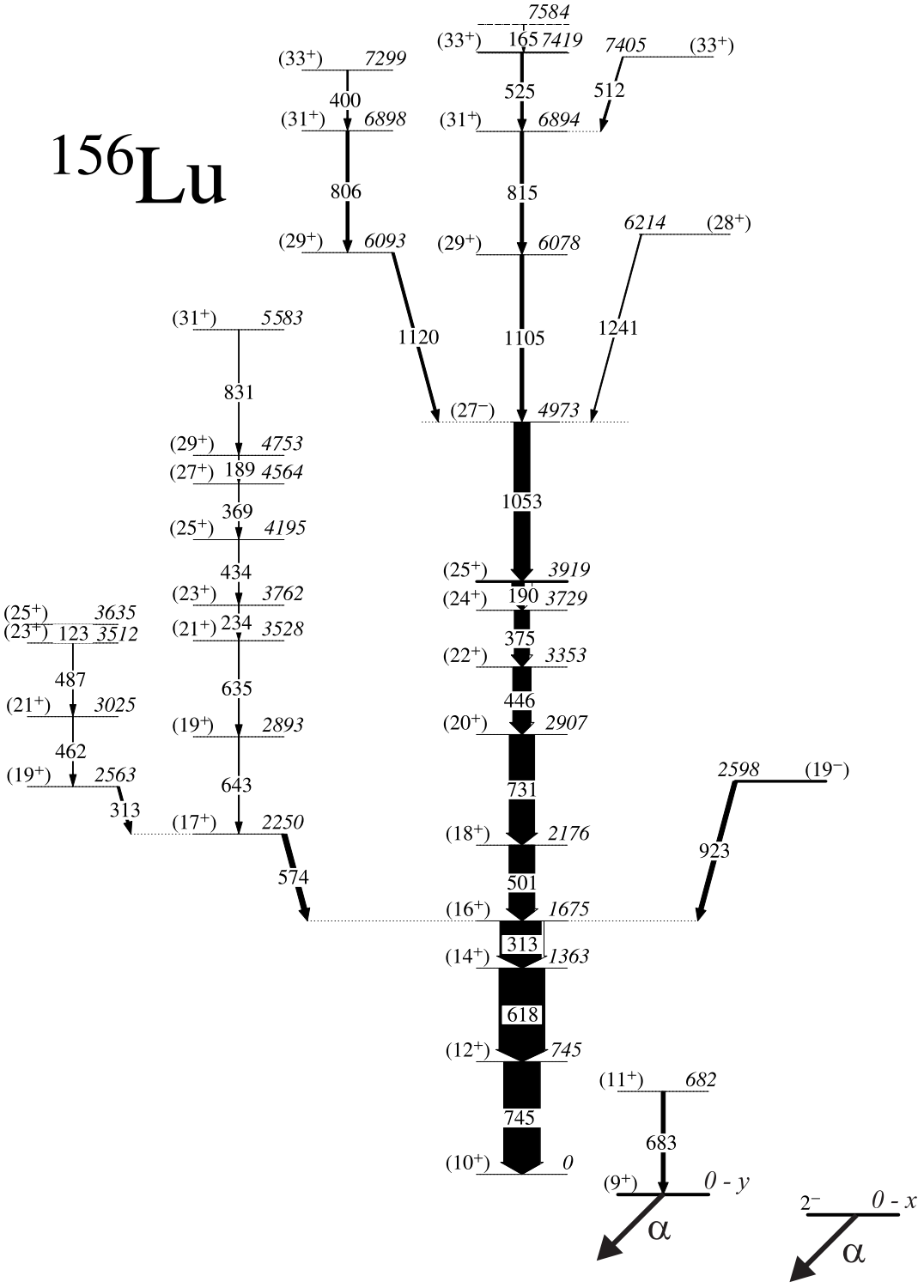

Figure 4.4: Level scheme deduced for the doubly-odd nucleus ^{156}Lu from the γ-ray coincidence analysis.

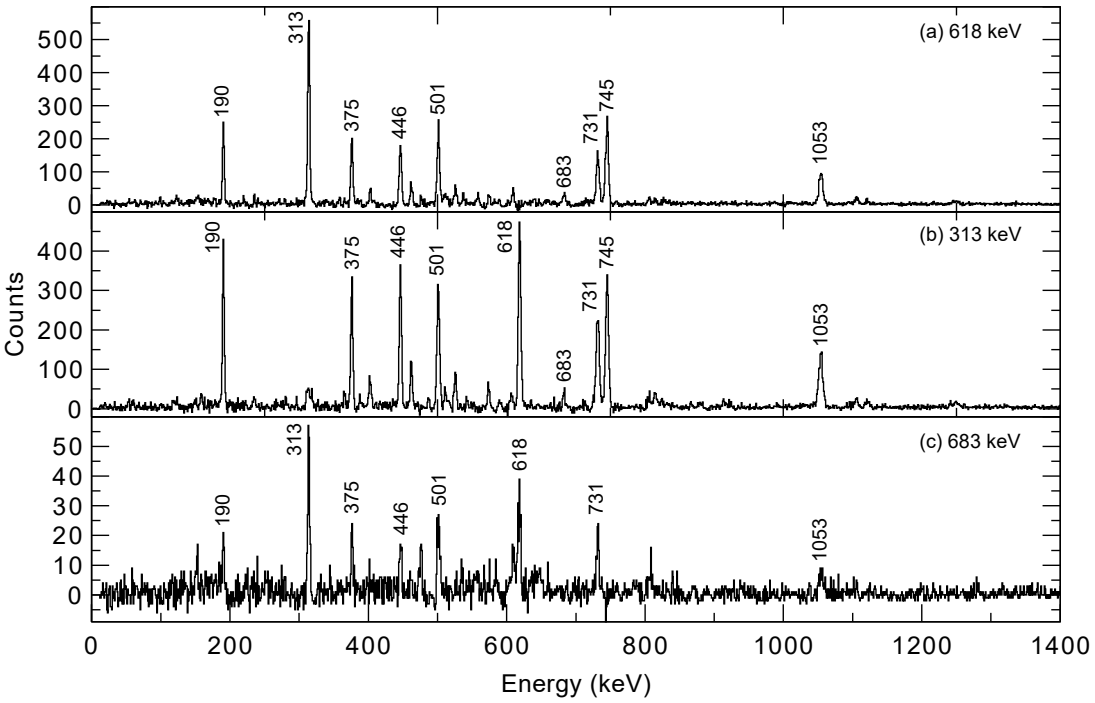

Figure 4.5: γ-ray coincidence spectra correlated with the α decay of the 9^+ state in ^{156}Lu. γ-rays demanded in coincidence with (a) 618 keV, (b) 313 keV and (c) 683 keV transition. The 683 keV transition is in coincidence with all transitions in the ^{156}Lu level scheme except for the 745 keV transition implying it is part of a parallel decay path.

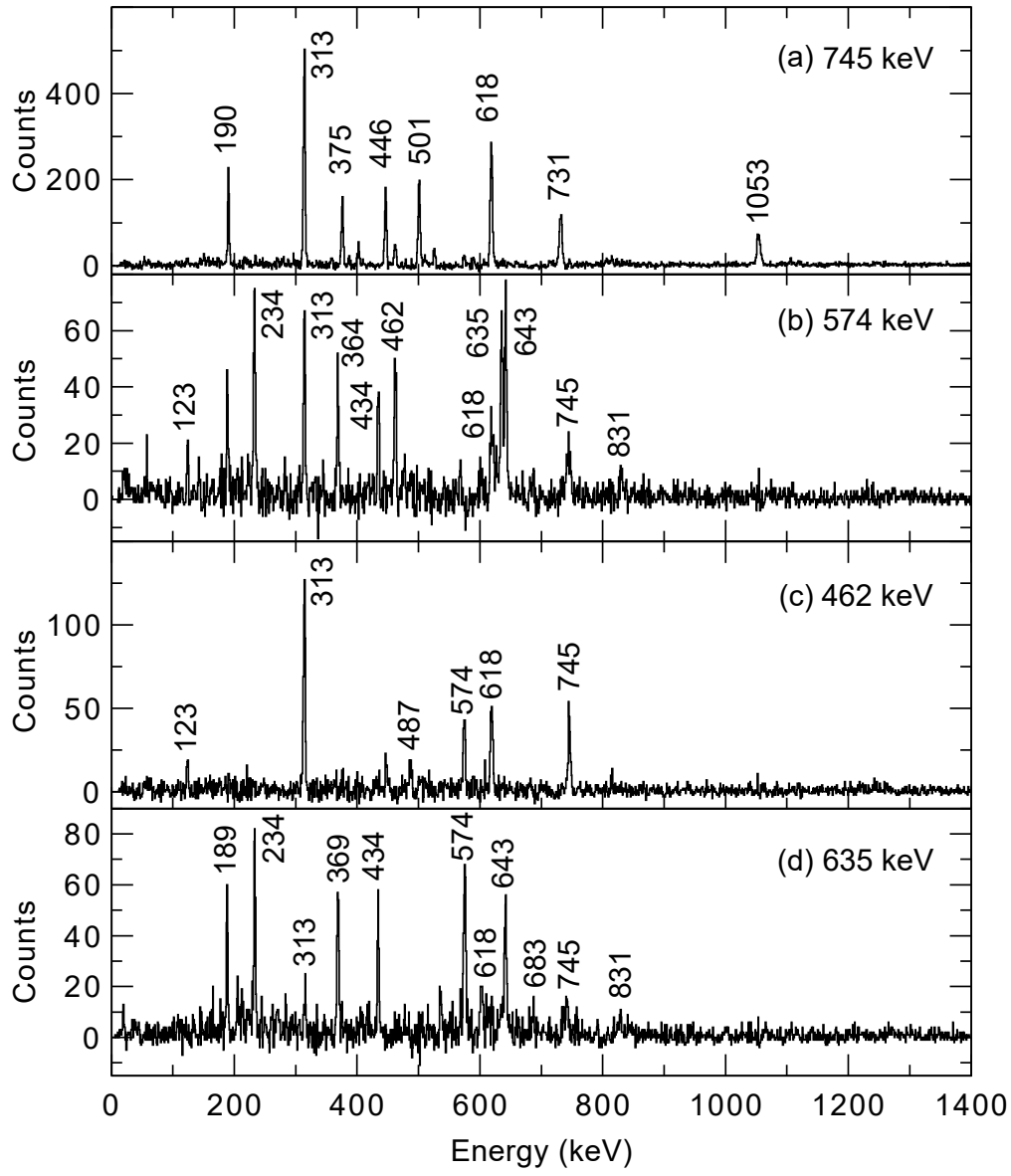

Figure 4.6: Typical γ-ray coincidence spectra correlated with the α decay from the 9^+ state in ^{156}Lu. Each spectrum is labelled by the γ-ray transition energy used to select coincidences.

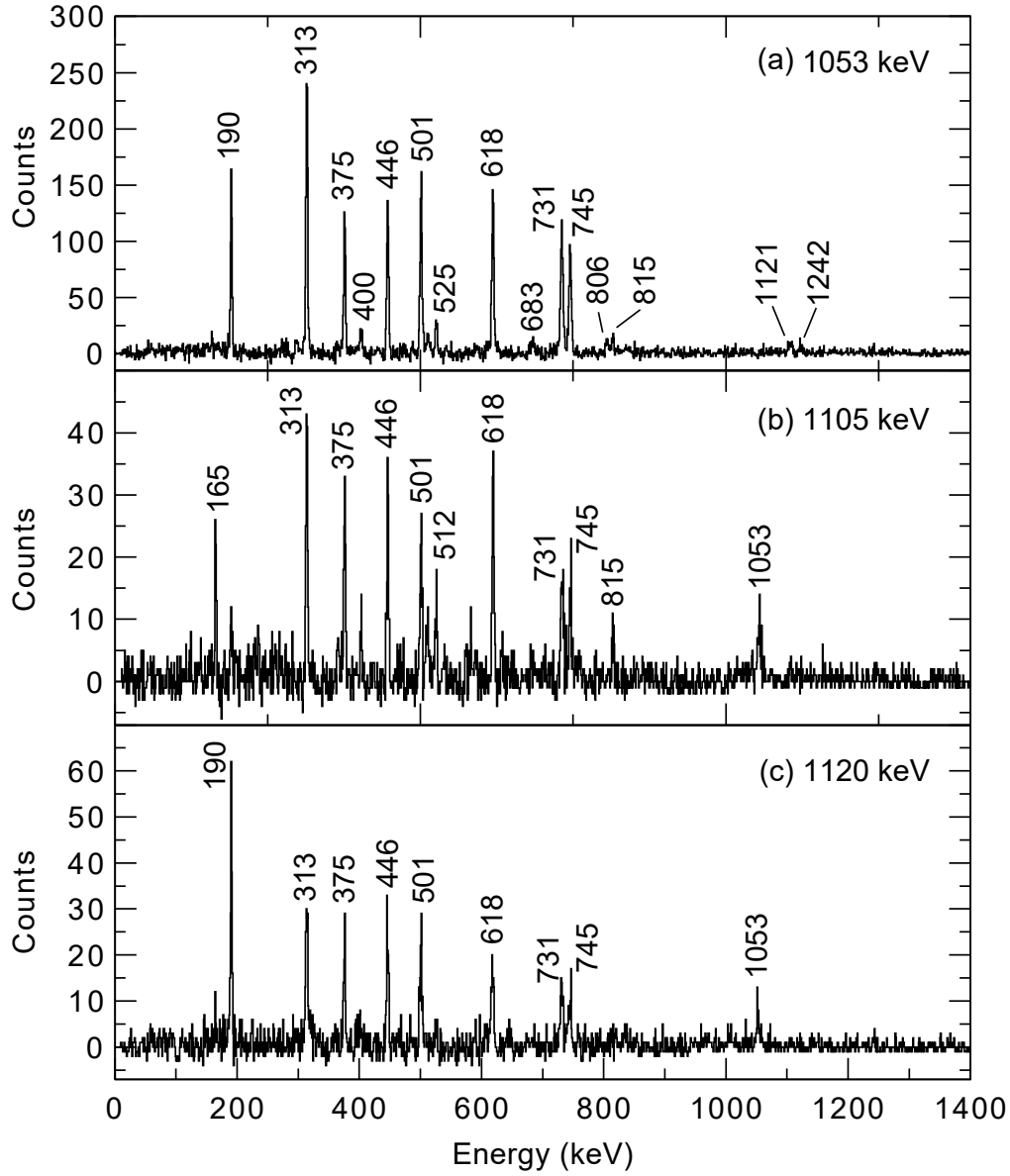

Figure 4.7: Further γ-ray coincidence spectra correlated with the α decay from the 9^+ state in ^{156}Lu. Each spectrum is labelled by the γ-ray transition energy used to select coincidences. These coincidences show the relationship between γ rays in the high-excitation energy region.

Some of the previously observed transitions that were assigned by Ding *et al.* [4] to feed the state depopulated by the 1053 keV transition such as the 190 keV, 375 keV and 446 keV γ rays have been reassigned as transitions between lower spin states. The remaining 400 keV and 525 keV γ rays have been assigned to the decay branches feeding the 1053 keV γ ray, which are associated with the groups of transitions 806 keV and 1120 keV, and the 165 keV, 815 keV and 1105 keV, respectively.

The relative intensities of the transitions in Figure 4.4 are hard to reconcile with a straightforward cascade. Indeed it was impossible to determine consistent relative intensity measurements using different coincidence spectra. However, since ^{156}Lu an odd-odd nucleus it is possible that there are one or more short-lived ($\sim$ns) isomeric states throughout the structure of this nucleus that are sufficiently long to interfere with intensity and angular distribution measurements. For example, the tentative (25^+) state that is depopulated by the 190 keV presumed E2 transition is predicted to have a 46 ns lifetime according to the Weisskopf estimates. The presence of any short-lived isomeric states means γ-ray emission could occur downstream of the target position and be detected with a lower efficiency, which is consistent with the measurements reported here. Table 4.4 lists the level and γ-ray transition properties observed in ^{156}Lu. The reader is advised to recall the above caveat about short-lived isomers when reviewing the relative intensity measurements in Table 4.4.

Table 4.3: Measured properties of energy levels and γ-ray transitions in ^{156}Lu. Level excitation energies are stated relative to the 10+ state. The intensities of the γ-rays are stated relative to the 618.1 keV transition.

Initial state excitation energy (keV)	J_i^π	$\rightarrow$	J_f^π	E_γ (keV)	Relative Intensity %
682	(11^+)	$\rightarrow$	(9^+)	683.0(10)	8.7(10)
745	(12^+)	$\rightarrow$	(10^+)	744.5(10)	80(19)
1363	(14^+)	$\rightarrow$	(12^+)	618.1(10)	100(21)
1675	(16^+)	$\rightarrow$	(14^+)	313.4(10)	91(24)
2176	(18^+)	$\rightarrow$	(16^+)	500.7(10)	56(14)
2250	(17^+)	$\rightarrow$	(16^+)	574.3(10)	11.2(10)
2563	(19^+)	$\rightarrow$	(17^+)	313.2(10)	5.1(10)
2598	(19^-)	$\rightarrow$	(16^+)	923.0(10)	10.0(10)
2893	(19^+)	$\rightarrow$	(17^+)	643.0(10)	2.2(10)
2907	(20^+)	$\rightarrow$	(18^+)	731.1(10)	56(11)
3025	(21^+)	$\rightarrow$	(19^+)	462.4(10)	1.5(10)
3353	(22^+)	$\rightarrow$	(20^+)	446.0(10)	40(10)
3512	(23^+)	$\rightarrow$	(21^+)	486.8(10)	0.3(10)
3528	(21^+)	$\rightarrow$	(19^+)	635.0(10)	2.0(10)
3635	(25^+)	$\rightarrow$	(23^+)	122.9(10)	0.2(10)
3729	(24^+)	$\rightarrow$	(22^+)	375.5(10)	32(10)
3762	(23^+)	$\rightarrow$	(21^+)	234.1(10)	1.5(10)
3919	(25^+)	$\rightarrow$	(24^+)	190.0(10)	28(11)
4195	(25^+)	$\rightarrow$	(23^+)	433.8(10)	1.1(10)
4564	(27^+)	$\rightarrow$	(25^+)	368.5(10)	1.0(10)
4753	(29^+)	$\rightarrow$	(27^+)	188.6(10)	0.7(10)
4973	(27^+)	$\rightarrow$	(25^+)	1053.3(10)	35(7)
5583	(31^+)	$\rightarrow$	(29^+)	830.9(10)	0.7(10)
6078	(29^+)	$\rightarrow$	(27^+)	1105.4(10)	8.1(10)
6093	(29^+)	$\rightarrow$	(27^+)	1119.7(10)	5.6(10)
6214	(29^+)	$\rightarrow$	(27^+)	1240.6(10)	2.4(10)
6894	(31^+)	$\rightarrow$	(29^+)	815.3(10)	7.4(10)
6898	(31^+)	$\rightarrow$	(29^+)	805.6(10)	6.6(10)
7299	(33^+)	$\rightarrow$	(31^+)	400.3(10)	3.1(10)
7419	(33^+)	$\rightarrow$	(31^+)	524.9(10)	5.7(10)
7435	(33^+)	$\rightarrow$	(31^+)	541.7(10)	4.7(10)

4.3.3 GREAT $\gamma\gamma$ coincidence analysis

It is possible to search for isomer-delayed γ-ray transitions at the focal plane of the RITU separator using the planar and clover detectors of the GREAT spectrometer. Figures 4.8 and 4.9 show γ-ray transitions detected at the focal plane and tagged by recoil-decay correlations for the clover and planar detectors, respectively. The recoil correlated spectra indicate that there are many γ ray transitions that occur as part of the de-excitation process from isomers that survive the flight time through the separator.

γ-ray coincidences detected at the separator focal plane and correlated with the characteristic α decay of the 9^+ state in ^{156}Lu were sorted into matrices. Planar-clover and clover-clover γ-ray coincidences were sorted into coincidence matrices. Figures 4.10 and 4.11 show typical coincidence spectra. Figure 4.10 shows the planar γ-ray spectrum obtained by demanding coincidences with the 745 keV transition in ^{156}Lu that were measured in the clover detector. The planar detector has a relatively poor detection efficiency above 500 keV, however the 313 keV ($16^+ \rightarrow 14^+$) transition is clearly seen. Clover γ-ray spectra extracted by demanding coincidences with the 313 keV transitions detected in the planar detector reveal γ rays with transition energies 618 keV, 745 keV and 923 keV. The 618 keV and 745 keV γ rays correspond to the known ($14^+ \rightarrow 12^+$) and ($12^+ \rightarrow 10^+$) transitions, respectively and are seen clearly by the JUROGAM II spectrometer at the target position. The 923 keV transition is detected exclusively by the focal plane clover detectors. The 923 keV, 313 keV, 618 keV and 745 keV transitions are assigned to decay directly from a high-spin isomeric state on the basis of these coincidences. The 923 keV γ ray is assigned to link the previously unknown isomeric state in ^{156}Lu to the 16^+ state.

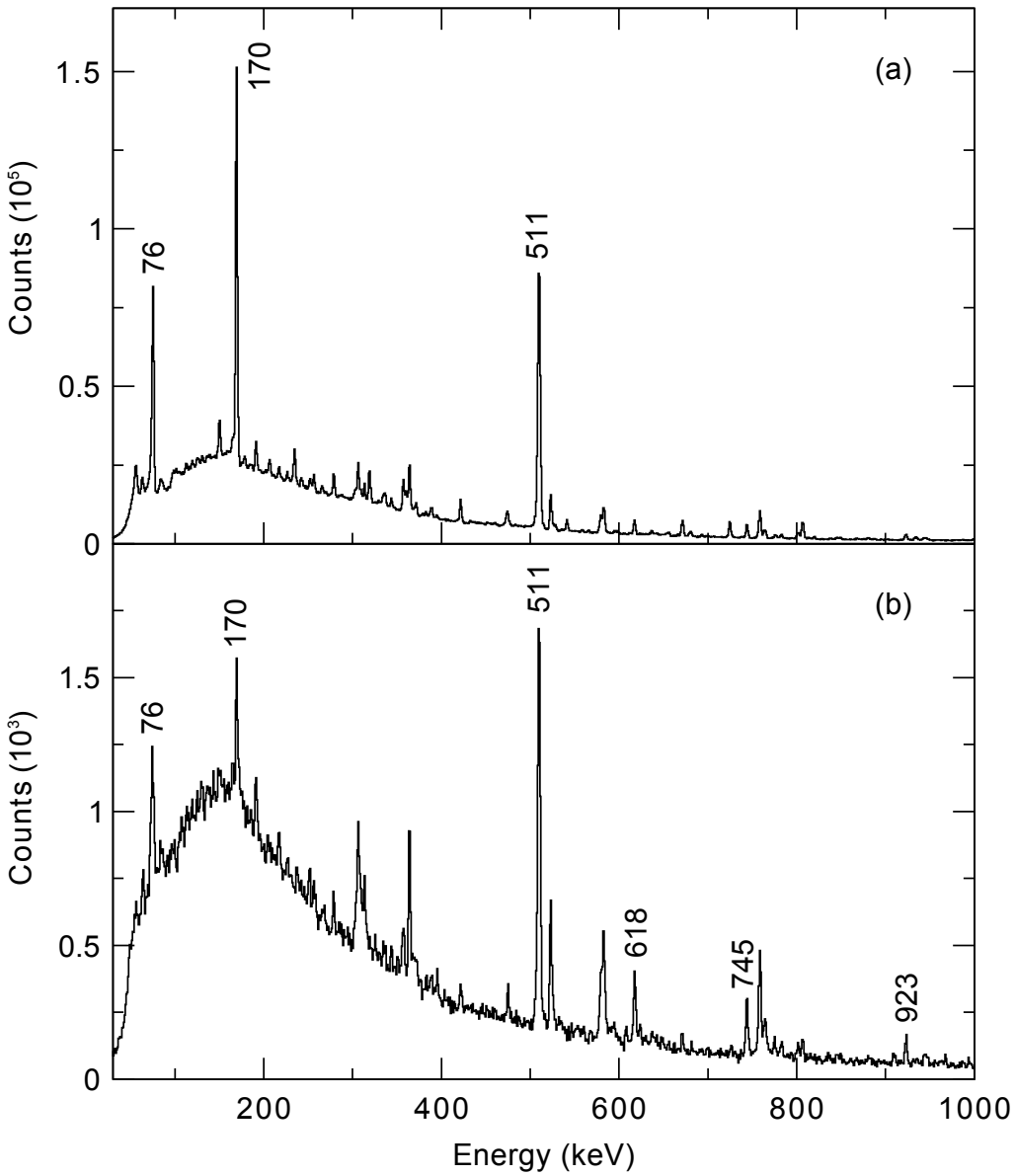

Figure 4.8: (a) γ-ray spectra detected with the GREAT clover detector at the focal plane of the recoil separator. These γ rays are correlated with recoil implantations in the GREAT DSSDs. (b) γ-ray spectra detected with the GREAT clover detector at the focal plane of the recoil separator. These γ rays are correlated with recoil implantations that are followed by the characteristic α decay of the 9^+ state in ^{156}Lu within the same pixel of the GREAT DSSDs. The correlation time for recoil-decay correlations was limited to 10 s.

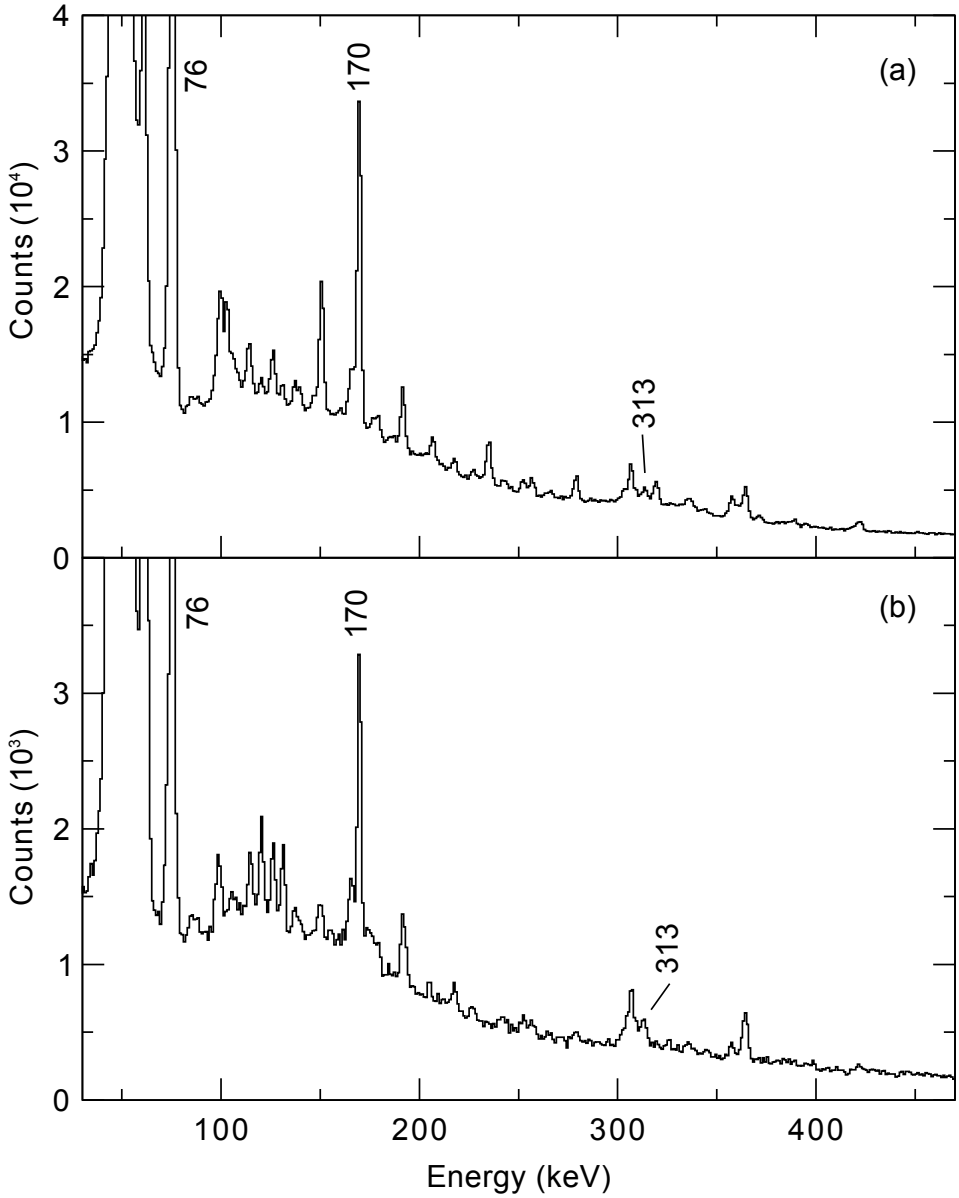

Figure 4.9: (a) γ-ray spectra detected with the GREAT planar detector at the focal plane of the recoil separator. These γ rays are correlated with recoil implantations in the GREAT DSSDs. (b) γ-ray spectra detected with the GREAT planar detector at the focal plane of the recoil separator. These γ rays are correlated with recoil implantations that are followed by the characteristic α decay of the 9^+ state in ^{156}Lu within the same pixel of the GREAT DSSDs. The correlation time for recoil-decay correlations was limited to 10 s.

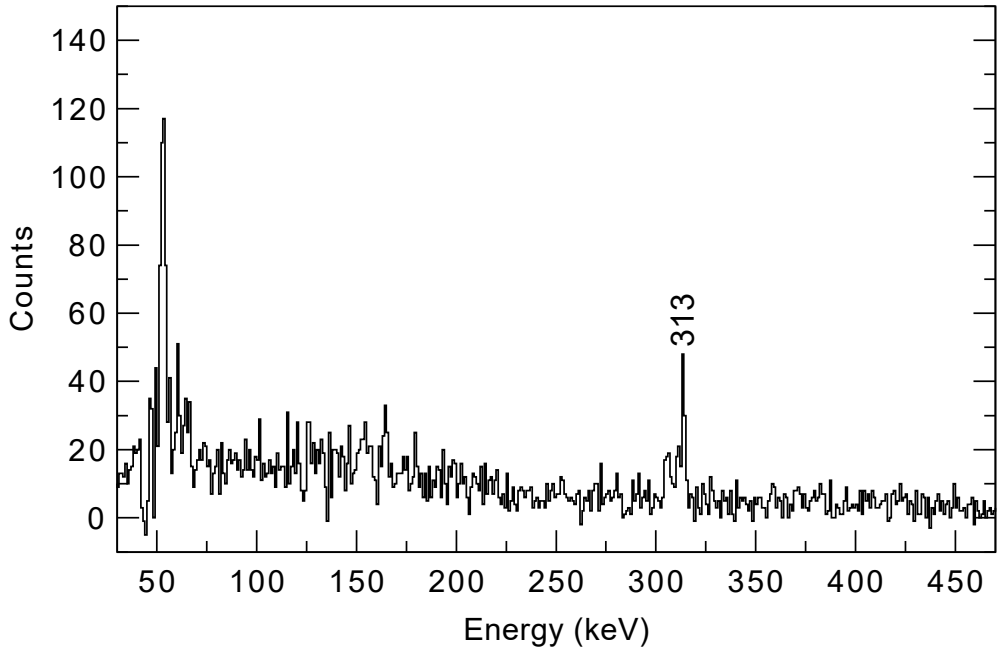

Figure 4.10: γ-ray coincidences generated from a recoil-decay tagged clover-planar γ-ray coincidence matrix. These γ rays are correlated with recoil implantations that are followed by the characteristic α decay of the 9^+ state in ^{156}Lu within the same pixel of the GREAT DSSDs. The correlation time for recoil-decay correlations was limited to 10 s. This spectrum shows γ rays in the planar detector obtained by demanding prompt coincidences with the 745 keV transition detected in clover detector.

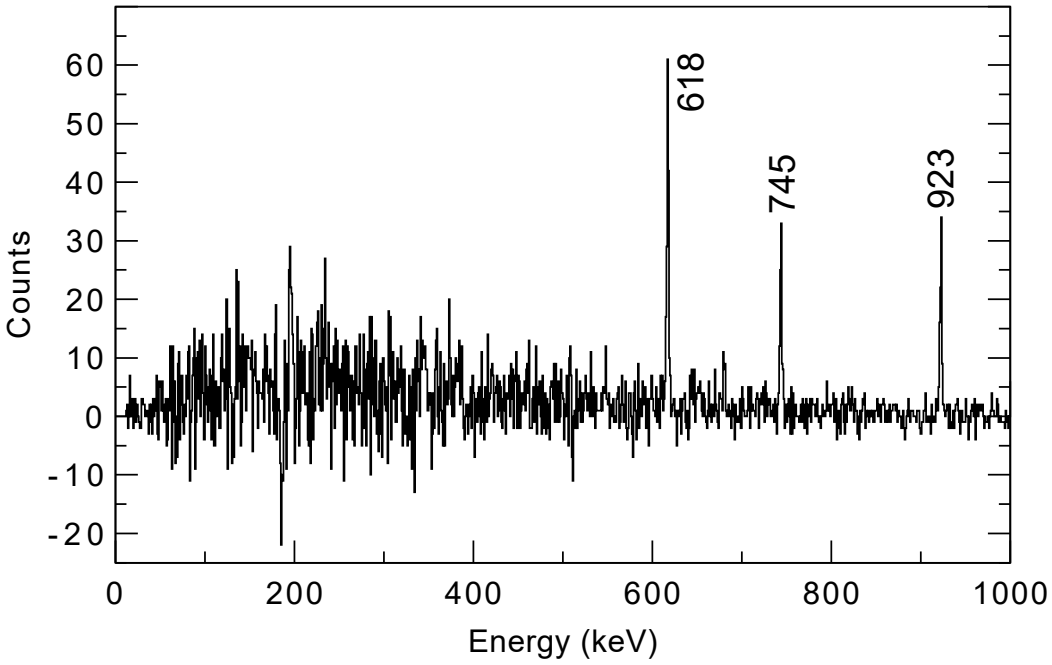

Figure 4.11: γ-ray coincidences generated from a recoil-decay tagged clover-planar γ-ray coincidence matrix. These γ rays are correlated with recoil implantations that are followed by the characteristic α decay of the 9^+ state in ^{156}Lu within the same pixel of the GREAT DSSDs. The correlation time for recoil-decay correlations was limited to 10 s. This spectrum shows γ rays in the clover detector obtained by demanding prompt coincidences with the 313 keV transition detected in planar detector.

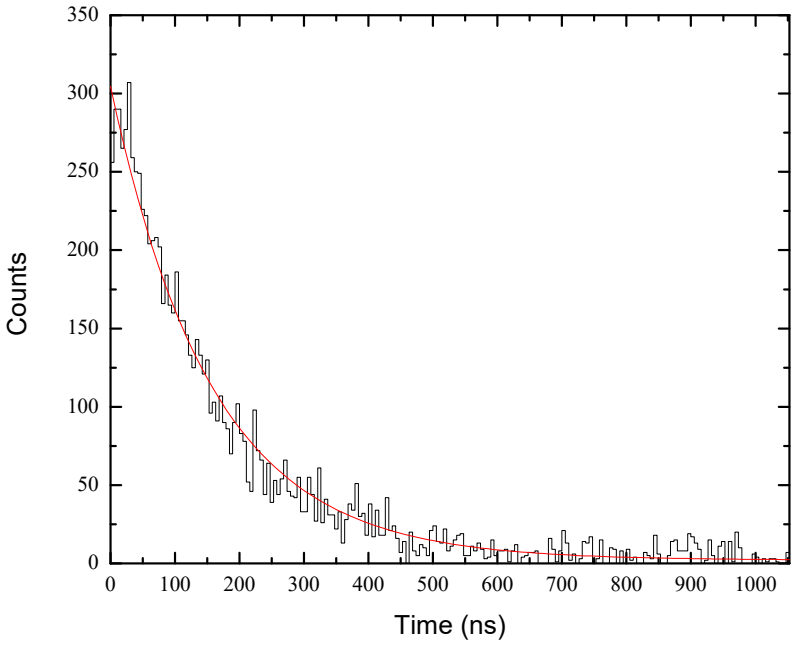

Figure 4.12: A background subtracted decay curve generated from the measured time differences between recoil implantations in the GREAT DSSDs and the 923 keV transition detected in the GREAT clover Ge detector. A half-life of 120(17) ns for the newly observed isomeric state in ^{156}Lu was obtained from an exponential fit to this decay curve. Time differences between subsequent recoils were extracted from the data. The recoil implantation rate is sufficiently low to limit the impact of false correlations on the measured lifetime.

The half-life of this isomeric state was measured from the time differences between implanted recoils in the DSSD and correlated ^{156}Lu γ rays detected in the focal plane clover and planar detectors, see Figure 4.12. A half-life of 120(17) ns for the newly observed isomeric state in ^{156}Lu was obtained from an exponential fit to this decay curve.

Recoil-isomer decay correlations were performed to tag γ rays detected at the target position by JUROGAM II in order to search for excited states above the new isomeric state. Figure 4.13 shows γ rays detected in JUROGAM II that were in delayed coincidence with the 313 keV, 618 keV, 745 keV or 923 keV transitions detected at the focal plane. The correlation times were limited to approximately three half-lives. Unfortunately the statistics required to produce a two-dimensional coincidence matrix are too low to reach any meaningful conclusions.

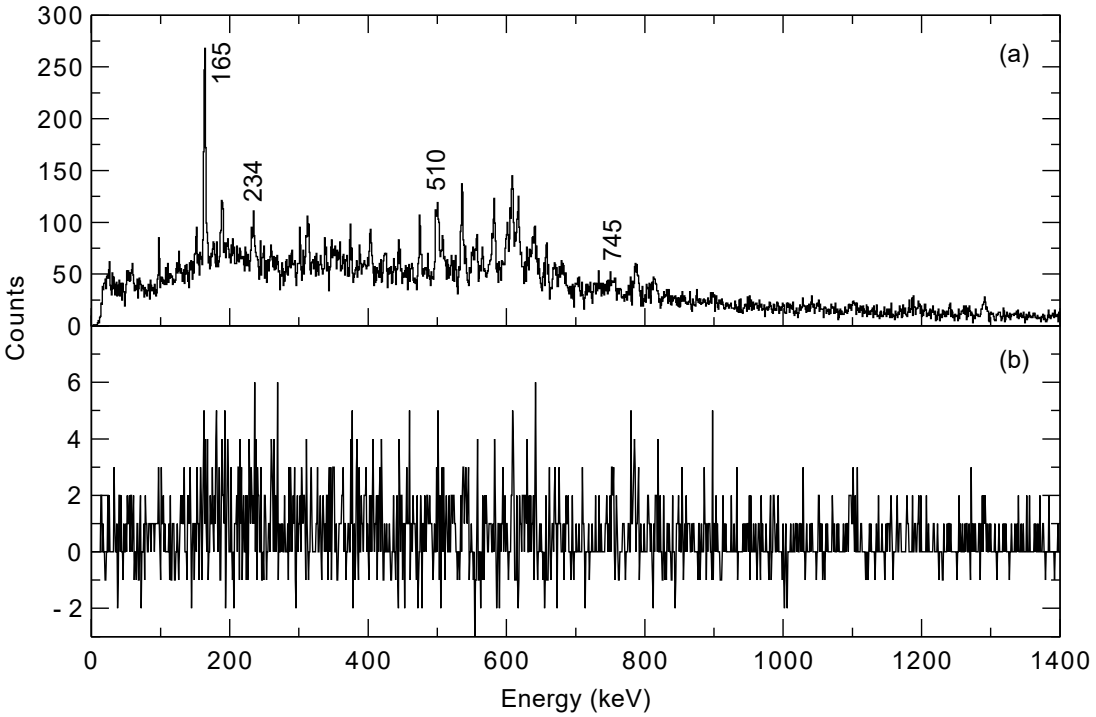

Figure 4.13: (a) γ rays measured at the target position with the JUROGAM II spectrometer that are in delayed coincidence with the 313 keV, 618 keV, 745 keV or 923 keV γ rays detected at the focal plane. The correlation time was limited to three times the half-life of 9^+ isomer in ^{156}Lu. A selection of peaks that may feed the new high-spin isomer have been labelled. (b) A projection from a isomer-decay tagged coincidence matrix shows there are too few statistics available to make meaningful measurements.

4.4 Discussion

The proton and neutron Fermi surfaces in ^{156}Lu are expected to lie close to the $\pi d_{3/2}$ and $\pi h_{11/2}$ and the $\nu f_{7/2}$, $\nu h_{9/2}$ and $\nu i_{13/2}$ orbitals, respectively. The angular momentum of the lowest-lying states in ^{156}Lu are expected to be generated by coupling the odd proton to various arrangements of the valence neutrons outside the $N = 82$ closed shell. The α-decaying ground state (2^-) and low-lying isomeric state (9^+) are expected to be formed by the $\pi d_{3/2} \otimes \nu f_{7/2}$ and $\pi h_{11/2} \otimes \nu f_{7/2}$, respectively. These configurations (and those discussed later) are labelled on the level scheme shown in Figure 4.14.

4.4.1 The low-lying states

It was noted earlier that a 683 keV transition is observed to be in coincidence with the 618 keV ($14^+ \rightarrow 12^+$) transition and other higher lying transitions but not with the 745 keV ($12^+ \rightarrow 10^+$) transition. This γ ray is assumed to be the $11^+ \rightarrow 9^+$ transition from the $\pi h_{11/2} \otimes \nu f^3_{7/2}$ multiplet that forms a parallel decay path to the 745 keV transition. Previous research into $N = 85$ isotones has revealed a systematic reduction in excitation energies of 10^+ state built upon the $\pi h_{11/2} \otimes \nu h_{9/2}$ configuration relative to 9^+ state built on the $\pi h_{11/2} \otimes \nu f_{7/2}$ configuration with increasing proton number, see Figure 4.15. The small energy difference between the 9^+ and 10^+ states as a function of proton number in the odd-odd $N = 85$ isotones is interpreted to arise from the attractive interaction between $\pi h_{11/2}$ and $\nu h_{9/2}$ orbitals, which increases as protons are added to the $\pi h_{11/2}$ orbital. The energy difference between the 9^+ and 10^+ states in ^{156}Lu could not be established in this work since it is assumed that the presumed M1 transitions that link the structures are highly converted or too low in energy to be detected with an appreciable efficiency.

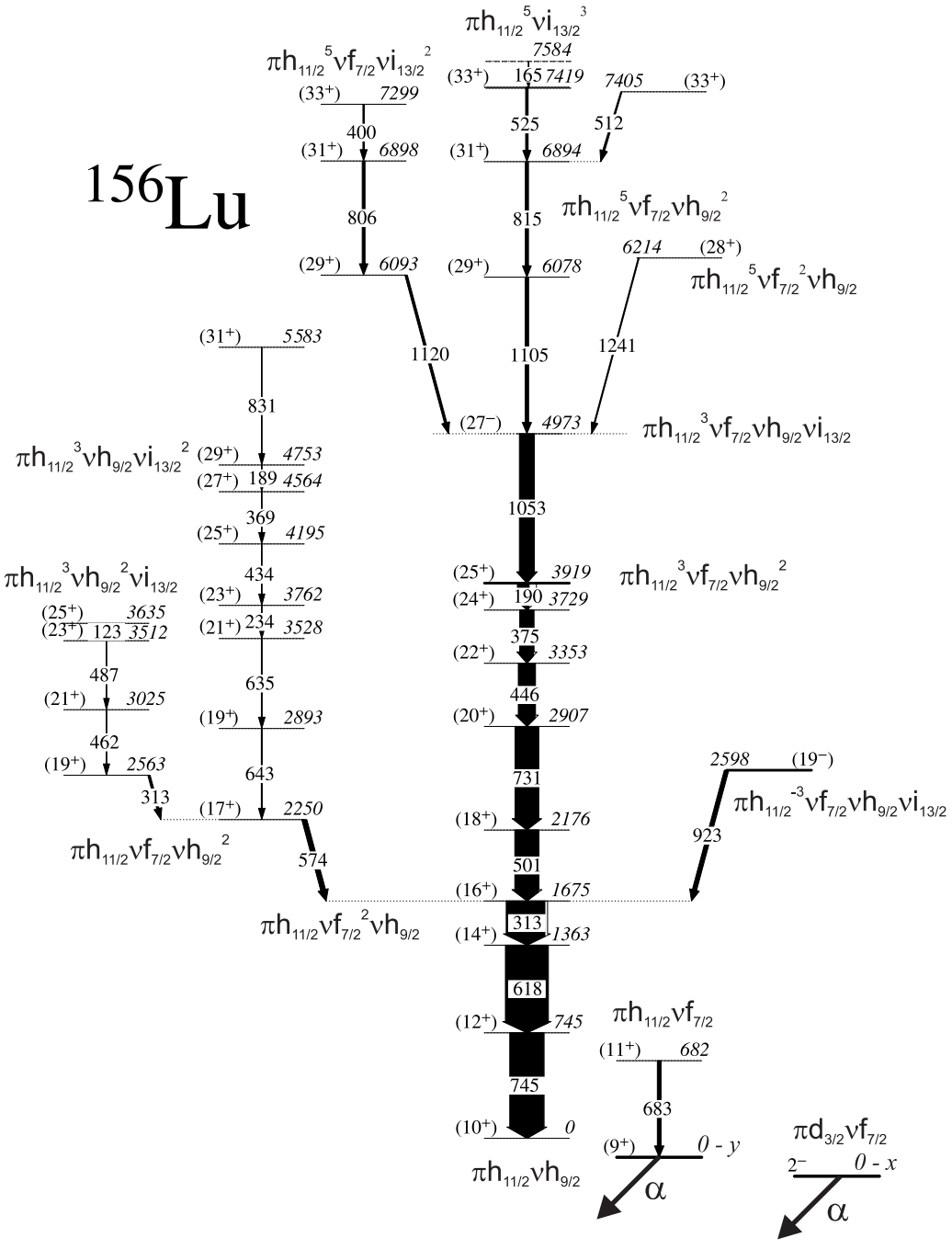

Figure 4.14: Level scheme for ^{156}Lu with configuration candidates labelled for fully aligned states. All the levels have tentative spin and parity assignments.

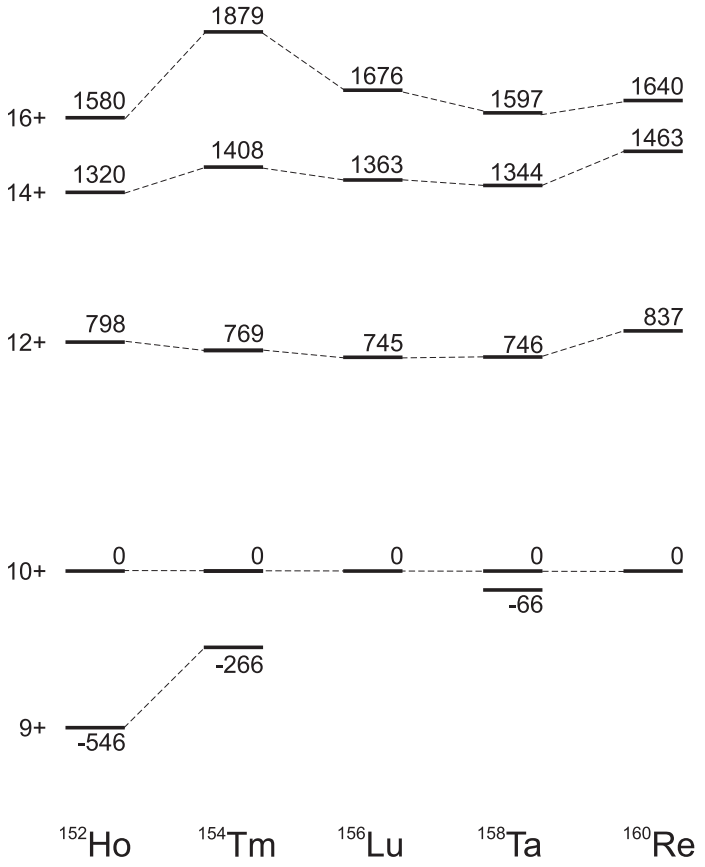

Figure 4.15: Excitation level systematics for the low-lying states in the $N = 85$ isotones. [43, 44, 45, 46, 47, 48, 49, 50]

The yrast states built upon the 10^+ state are expected from systematics to be assigned to the $\pi h_{11/2} \otimes \nu f_{7/2}^2 h_{9/2}$ configuration, which reaches it full alignment at the 16^+ state. Figure 4.15 shows the systematic trends of the low-lying states in the $N = 85$ isotones.

4.4.2 The excited states above the 17^+ state (E_i=2250 keV)

Several mechanisms exist for generating states with spins greater than 16^+. The next available excited multiplets could be generated by excitations involving different combinations of the $\pi h_{11/2}$, $\nu f_{7/2}$, $h_{9/2}$, and $i_{13/2}$ states. The lowest four quasiparticle configuration above spin 16^+ is presumed to be the $\pi h_{11/2} \otimes \nu f_{7/2} h^2_{9/2}$ state at 17^+. The cascades feeding the tentative 17^+ state could be formed by breaking a $\pi h_{11/2}$ pair and coupling to one or more neutrons into the $\nu i_{13/2}$ orbital; the $\pi h^3_{11/2} \otimes \nu h^2_{9/2} i_{13/2}$ configuration could give rise to a 23^+ state while higher spin states up to 29^+ could be achieved with the $\pi h^3_{11/2} \otimes \nu h_{9/2} i^2_{13/2}$ configuration. The 831 keV transition above the 4753 keV state is likely to be a pair-breaking transition to an excited six quasiparticle configuration.

4.4.3 The highest-spin states

The full alignment of six valence particles in the $\pi h^3_{11/2} \otimes \nu f_{7/2} h_{9/2} i_{13/2}$ configuration is expected to produce a state with spin and parity 28^-. In ^{152}Ho this state is isomeric with a 47 ns half-life and lies at 5838 keV while the ^{154}Tm and ^{158}Ta states at 6141 keV and 5273 keV could correspond to this configuration. In this work, the 27^- is assigned to this configuration in order to ensure lifetimes consistent with observing coincidences across this state. According to the Weisskopf estimates a 1053 keV M2 transition would have a lifetime of 0.3 ns compared with 80 ns for an E3 transition.

The level scheme above the assigned 27^- depopulated by the 1053 keV transition splits into three branches. Each branch begins with a high-energy γ ray. A mechanism for generating even higher spins is through the creation of higher-seniority states by breaking more pairs of $h_{11/2}$ protons and aligning their angular momenta with the neutrons remaining in $f_{7/2}$, $h_{9/2}$ and $i_{13/2}$ orbitals. Thus, the underlying

structure of the states at the highest excitation energies are assumed to be based on $\pi h^5_{11/2}$ configurations coupled to the available neutron states.

4.4.4 The 19^- isomeric state

The new isomeric state at an excitation energy of 2598 keV relative to the 10^+ state is assumed to have a similar character to the high-spin isomers observed in the other $N = 85$ isotones, ^{152}Ho [51] and ^{158}Ta [52]. The isomer in ^{156}Lu de-excites via the emission of a 923 keV γ ray to the 16^+ state with a measured half-life of 120(17) ns. The Weisskopf estimate for an E3 γ decay (2.1 μs) is the closest value to the measured lifetime. Thus, the isomer is assigned a spin and parity of 19^-. The isomers in N = 84 isotones ^{152}Ho and ^{158}Ta also decay via E3 transitions [51, 52].

The 19^- isomer is assigned to have the $\pi h^{-3}_{11/2} \otimes \nu f_{7/2} h_{9/2} i_{13/2}$ configuration in the other isotones. Andre *et al.* in their work on ^{152}Ho noted that this spin assignment cannot be obtained by the complete alignment of those six valence particles, which would result in a spin and parity of 20^- [51]. They propose a configuration for the isomer that was based on the fully aligned state of the three valence neutrons $[\nu f_{7/2}, h_{9/2}, i_{13/2}]_{29/2^+}$ is coupled to three protons in the $(j-1)_{9/2^-}$ state of the $\pi h^{-3}_{11/2}$ multiplet. The level inversion was assumed to arise from the non-aligned state having the largest quadrupole moment of the j^3 configuration, which when coupled to other states with high angular momentum results in an attractive residual interaction that depresses the $j-1$ state relative to other states in the multiplet. The excitation energy of the isomer relative to the 10^+ state is 2314 keV in ^{152}Ho, 2598 keV in ^{156}Lu and 2600 keV in ^{158}Ta does not provide any systematic behaviour that might shed light on these interactions as a function of proton number.

4.5 Results: ^{158}Lu

4.5.1 Identification of excited states in ^{158}Lu

The information available on the neutron-deficient nucleus ^{158}Lu is sparse. A single α-decay line was identified in earlier studies and the decay properties of ^{158}Lu are not well suited to recoil-decay tagging studies [37]. The α-decay branch is only 0.91 % with electron capture being the dominant decay branch at 99.09 %. Dracoulis *et al.* identified some γ rays in ^{158}Lu that depopulated excited states following a fusion evaporation reaction. The assignment of these γ rays to ^{158}Lu relied on γ-X-ray coincidences. To date no level scheme has been published in the literature.

In this work, γ rays have been assigned to ^{158}Lu using isomer-decay tagging on the 76 keV and 170 keV isomeric states. The 5pn reaction channel leading to ^{158}Lu was a strong reaction channel, which allowed the opportunity for well constrained channel selection, therefore building a level scheme using E_{γ_1}-E_{γ_2}-E_{γ_3} coincidence analysis. For additional proof of principle, γ rays were detected in the JUROGAM II spectrometer and in coincidence with five-fold particle evaporations in the LISA detector, as Figure 4.16 shows. The particle-γ correlations select the yrast sequence previously identified by Dracoulis *et al.* [38] and confirm the assignment of these γ rays to ^{158}Lu.

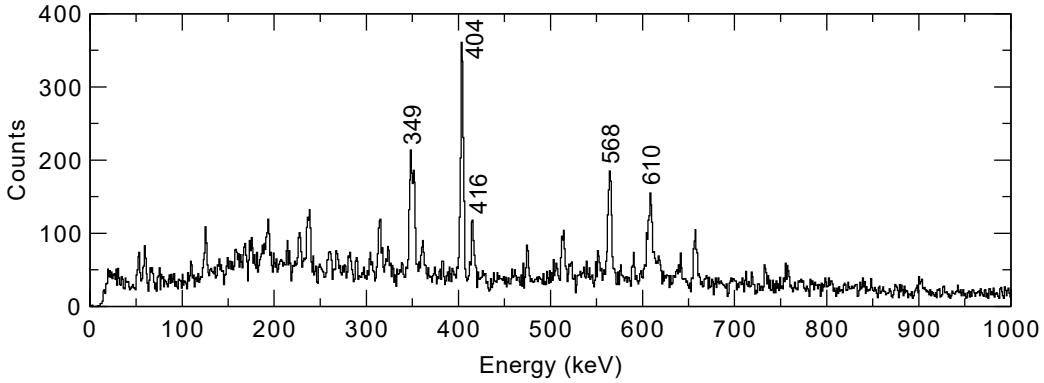

Figure 4.16: γ rays detected in the JUROGAM II spectrometer and in coincidence with five-fold particle evaporations in the LISA detector. The γ rays assigned to ^{158}Lu by Dracoulis *et al.* [38] are prominent in the spectrum.

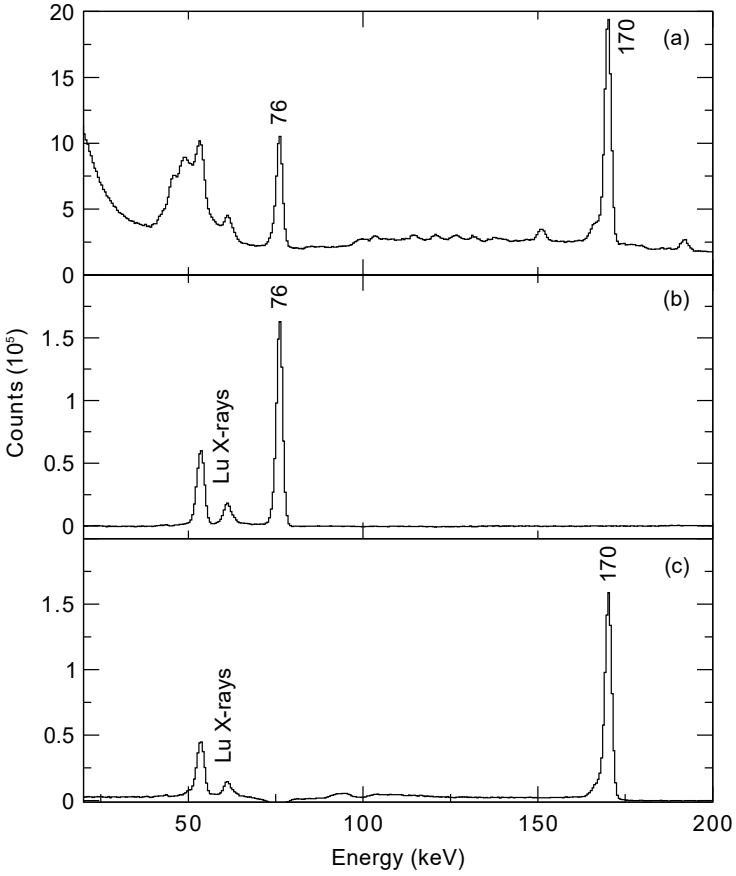

Figure 4.17: (a) displays a projection from a $\gamma-\gamma$ coincidence matrix generated from the GREAT planar detector with γ rays that are detected within 200 ns of a recoil implantation in the GREAT DSSD. (b) γ and X-rays in prompt coincidence with the 170 keV γ ray. (c) γ and X-rays in prompt coincidence with the 76 keV γ ray. The spectra shown in (b) and (c) are background subtracted.

4.5.2 Focal plane $\gamma - \gamma$ coincidences

The focal plane Ge detectors of the GREAT spectrometer were used to search for decays from isomeric states. A new isomeric state was observed in this work. γ-ray coincidences measured in the Ge detectors of the GREAT spectrometer reveal that the de-excitation path from this isomer comprises at least two γ rays at 76 keV and 170 keV, see Figure 4.17. These γ rays are in coincidence with the characteristic Lu X-rays confirming the atomic number to be $Z = 71$.

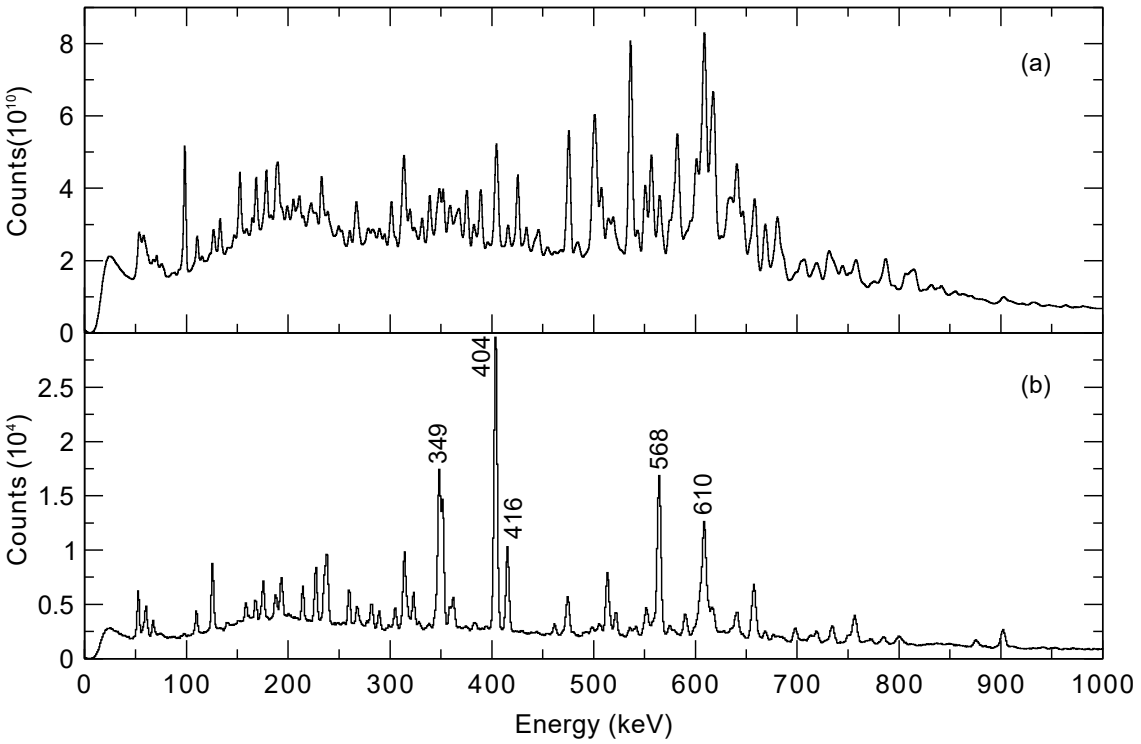

Figure 4.18: (a) γ-rays detected at the target position by JUROGAM II and correlated with a recoil implantation in the GREAT DSSD detectors at the focal plane. (b) γ rays detected in delayed coincidence with recoil implantations in the GREAT spectrometer and followed by the 76 keV or 170 keV isomer-delayed γ-ray transitions.

Recoil-isomer correlations were performed using these γ rays as a tag to select γ-ray transitions detected in the JUROGAM II spectrometer at the target position. Figure 4.18 compares γ rays detected in delayed coincidence with recoil implantations in the GREAT spectrometer with spectra generated by demanding the additional constraint of detecting either the 76 keV or 170 keV transition from the isomer's decay path. A sequence of γ rays previously assigned as the yrast states in ^{158}Lu by Dracoulis *et al.* [38] are clearly identified in the isomer-decay correlated spectrum. Thus, the isomer and the γ rays that de-excite it are assigned to ^{158}Lu on the basis of these correlations.

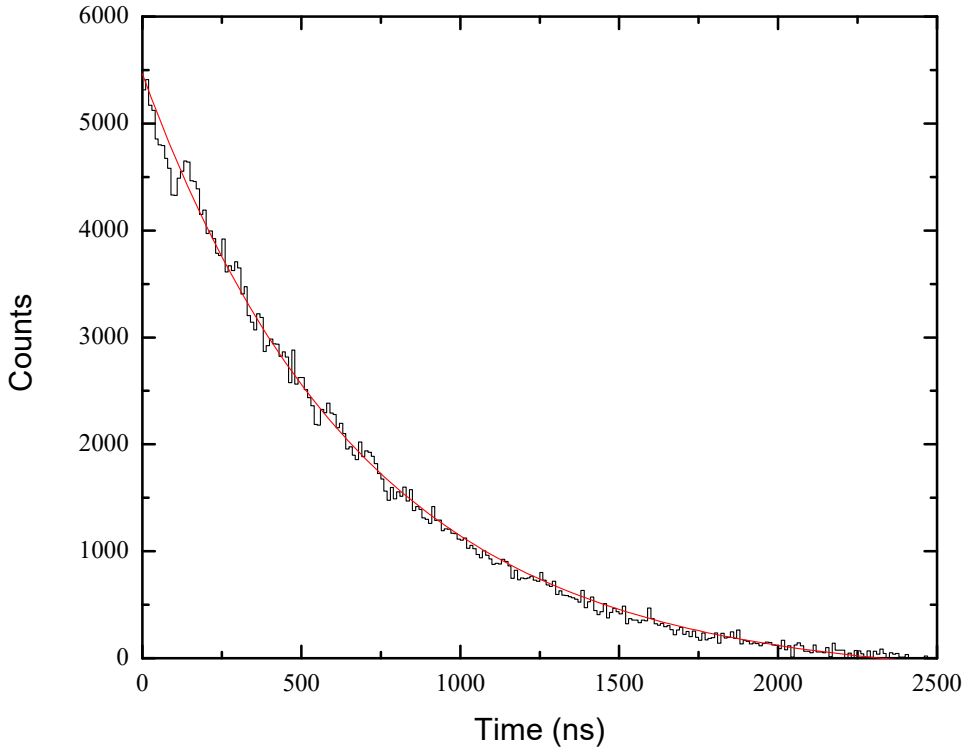

Figure 4.19: A background subtracted decay curve generated from the measured time differences between recoil implantations in the GREAT DSSDs and the 170 keV transition detected in the GREAT spectrometer. A half-life of 456(2) ns for the newly observed isomeric state in ^{158}Lu was obtained from a fit to this decay curve.

Figure 4.19 shows a background subtracted decay curve generated from the measured time differences between recoil implantations in the GREAT DSSDs and the 170 keV transition detected in the GREAT spectrometer. A half-life of 456(2) ns for the newly observed isomeric state in ^{158}Lu was obtained from a fit to this decay curve. The corresponding lifetime $\tau \sim 660\ ns$, which is the same order of magnitude at the Weisskopf estimates of a 170 keV E2 transition.

Further information on the multipolarities of the isomer-delayed transitions can be obtained by measuring the conversion coefficient α_{tot}. The conversion coefficients can be obtained by using γ- and X-ray intensity information measured from Figure 4.17 and assuming a simple two-step cascade. These data can be substituted into the equation

Table 4.5: Internal Conversion Coefficients calculations for the isomer in ^{158}Lu using X-rays and γ rays from transitions fed by the isomeric state.

	Energy	Area	Efficiency	Intensity	K-ICC	ICC_{tot}
K_α	54.1(1)	266090(515)	24.14(2.41)	64234(6424)	0.78(13)	0.717(1)
K_β	61.3(1)	82760(287)	24.36(2.43)	20160(2017)		
γ	170	862486(928)	12.6(1.26)	108673(10867)		
K_α	54.1(1)	405824(637)	24.14(2.41)	97965(9797)	0.60(10)	0.845(1)
K_β	61.3(1)	105700(325)	24.36(2.43)	25748(2576)		
γ	76	848272(921)	24.12(2.41)	204603(20461)		

$$\alpha_K = \frac{I_X^K}{\omega_f I_\gamma}, \tag{4.1}$$

where I_X^K is the summed intensity of the K_α and K_β X rays, I_γ is the γ-ray intensity and ω_f is the fluorescence yield [53]. The fluorescence yield was assigned to be 0.9369 from Hagedoorn and Wapstra [54]. The peak areas and deduced intensities of the K_α, K_β and γ rays were measured and recorded in Table 4.5. The total internal conversion coefficient was obtained using

$$I_{tot} = I_\gamma(1 \ + \ \alpha_{tot}). \tag{4.2}$$

The value obtained for the 76 keV transition, α_{tot}=0.845(1), compares favourably to the theoretical value of α_{tot}=0.7135 for an E1 transition obtained from BRICC [14]. The measured conversion coefficient for the 170 keV transition α_{tot}=0.717(1) is similar to the BRICC theory predictions for M1 (α_{tot}=0.8149) and E2 (α_{tot}=0.4824) transitions. This is consistent with the multipolarity deduced from the measured half-life for the isomer decay. On the basis of these measurements, the 170 keV transition is assigned to have an E2 multipolarity (possibly E2/M1) and presumed to de-excite the isomeric state. The 76 keV transition is assigned to be an E1 transition.

4.5.3 JUROGAM II $\gamma\gamma$ coincidence analysis

The 76 keV and 170 keV γ rays detected at the focal plane in the GREAT spectrometer can be used as a selective tag on γ rays detected at the target position, see Figure 4.18. Both an isomer-decay correlated E_{γ_1}-E_{γ_2} matrices and a E_{γ_1}-E_{γ_2}-E_{γ_3} cube were sorted from the data and analysed to deduce the level scheme shown in Figure 4.20. Typical coincidence spectra obtained from a 76 keV and 170 keV isomer-decay correlated E_{γ_1}-E_{γ_2}-E_{γ_3} cube are shown in Figure 4.21.

The yrast sequence beginning with the 404 keV intensity is likely to be based on a short-lived isomer. The coincidence relationships between the 404 keV γ ray (and higher-lying transitions) and the 126 keV, 194 keV and 659 keV γ rays suggest there is a loss of intensity in the latter group. The lower intensity of the 659 keV and associated γ rays could arise if the state fed by the 404 keV transition has a lifetime of approximately 10 ns.

The level scheme for ^{158}Lu is shown in Figure 4.20. The properties of excited states above the isomer and the associated γ-ray transitions are listed in Table 4.6.

Table 4.6: The level scheme for ^{158}Lu can be considered in three parts: the decay path from the 456(2) ns isomer to the ground state, the low-intensity states immediately above the 456(2) ns isomer and the high-spin yrast states.

Initial state excitation energy (keV)	J_i^π	$\rightarrow$	J_f^π	E_γ (keV)	Relative Intensity %
0-z+76	(1^+)	$\rightarrow$	(2^-)	76.0(10)	1.0(10)
0-x+126				126.2(10)	15.7(2)
0-y+170	(8^+)	$\rightarrow$	0−y	170.0(10)	0.5(10)
404	(13^-)	$\rightarrow$	(11^-)	404.5(10)	100.0(8)
619				214.8(10)	7.6(2)
0-x+465				194.0(10)	10.2(2)
0-x+659				658.6(10)	26.9(4)
928				523.5(10)	9.0(2)
970	(15^-)	$\rightarrow$	(13^-)	565.0(10)	81.6(8)
1318				349.0(10)	43.7(6)
1579				260.4(10)	9.7(2)
1579	(17^-)	$\rightarrow$	(15^-)	609.4(10)	76.0(8)
1931	(19^-)	$\rightarrow$	(17^-)	352.2(10)	42.3(6)
2347	(21^-)	$\rightarrow$	(19^-)	415.9(10)	35.7(4)
2585				237.9(10)	29.4(3)
2709				362.2(10)	15.9(3)
3060				475.2(10)	25.0(4)
3105				757.6(10)	22.1(4)
3420				315.0(10)	28.6(6)
3743				323.7(10)	13.9(2)
3963				902.9(10)	21.0(4)
4478				734.8(10)	16.0(3)

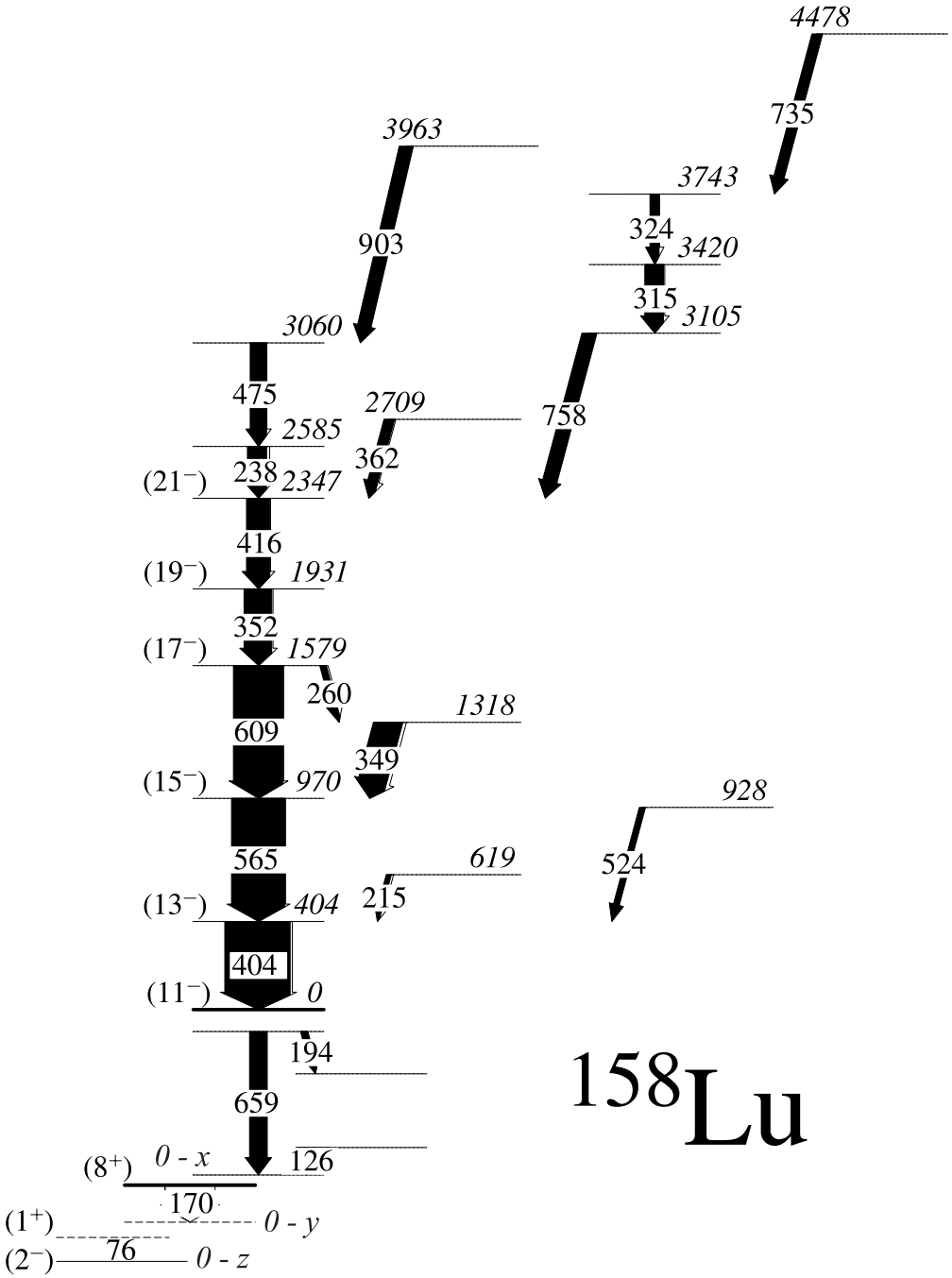

Figure 4.20: Level scheme deduced for ^{158}Lu. Level excitation energies are quoted relative to the (11^-) state. The arrow widths of γ-ray transitions above the (8^+) isomer are proportional to the relative intensities. The relative intensities are normalised to the intensity of the 404 keV transition.

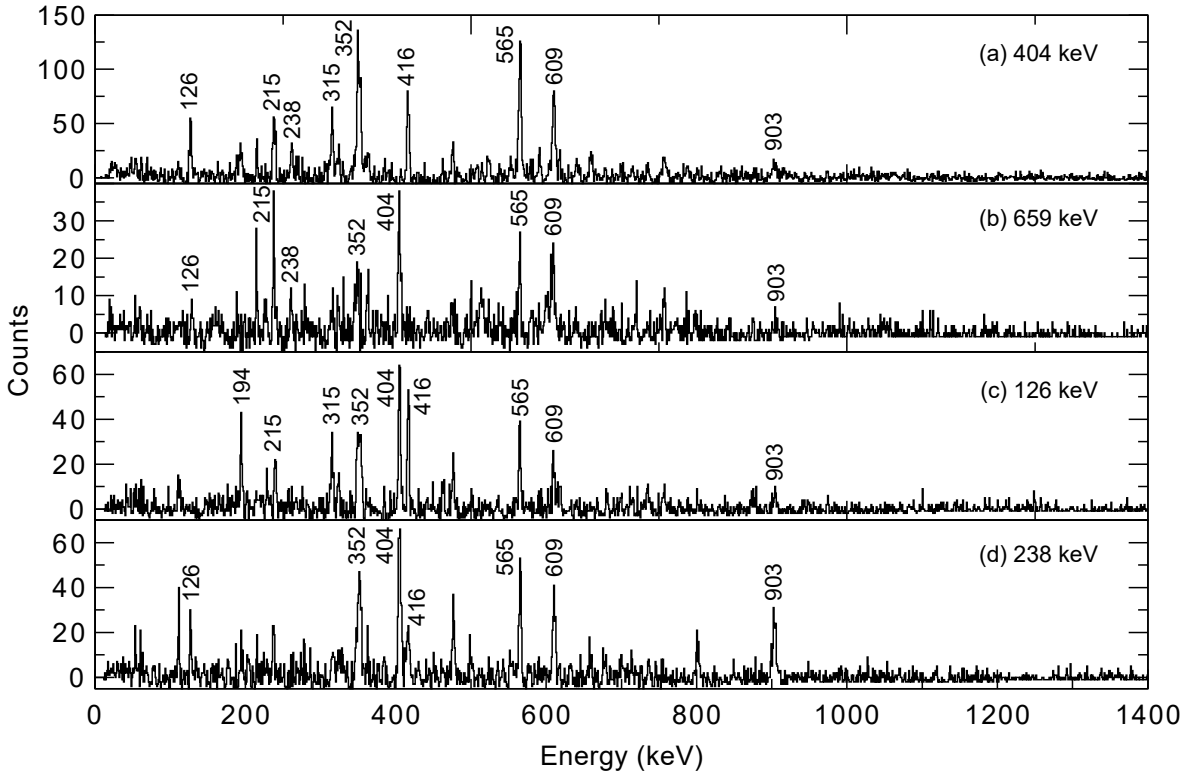

Figure 4.21: Typical γ-ray coincidence spectra obtained from a 76 keV and 170 keV isomer-decay correlated $\gamma - \gamma - \gamma$ cube.

4.6 Discussion

The proton and neutron Fermi surfaces in ^{158}Lu, like the lighter odd-odd isotope ^{156}Lu, are expected to lie close to the $\pi d_{3/2}$ and $\pi h_{11/2}$ and the $\nu f_{7/2}$, $\nu h_{9/2}$ and $\nu i_{13/2}$ orbitals, respectively. The angular momentum of the lowest-lying states in ^{156}Lu are expected to be generated by coupling the odd proton to various arrangements of the five valence neutrons outside the $N = 82$ closed shell. The increased valence space allows a degree of collective behaviour to develop but the single-particle excitations remain important.

4.6.1 The decay path from the 456(2) ns isomer to the ground state.

The ground state in ^{158}Lu is expected to be a 2^- state formed by the anti-parallel coupling of the odd $d_{3/2}$ proton with the odd $f_{7/2}$ neutron. The first excited states in the $N = 87$ isotones have been investigated in the electron capture of the even-Z precursors and assigned as 1^+ configurations. For example, the lighter odd-odd isotones ^{156}Tm [55] and ^{154}Ho [56, 57] have excited 1^+ states at excitation energies of 115 keV and 26 keV, respectively, relative to their 2^- ground states [58]. The 1^+ state could arise from the anti-parallel coupling of the $h_{11/2}$ protons and $h_{9/2}$ neutrons [59].

The 76 keV transition has been assigned as an electric dipole $1^+ \rightarrow 2^-$ transition. The 170 keV transition is consistent with an E2 transition depopulating the 456(2) ns isomer. It is possible that the new isomeric state in ^{158}Lu corresponds to the 8^+ isomer observed in the lighter $N = 87$ isotones [55, 56, 57, 60]. The 8^+ isomeric configuration has been interpreted to arise from the coupling of the $[\nu f_{7/2}^3]_{5/2}$ neutron state to the odd proton in the $h_{11/2}$ orbital [60].

Assuming that the 456(2) ns isomer is the 8^+ isomer, the multipolarity assign-

ment of the 76 keV and 170 keV transitions cannot span the angular momentum difference to the 2^- ground state. Sequences of low-energy transitions are hard to detect between low-spin states in odd-odd nuclei. For example, the recent work investigating ^{160}Re [61, 62] has verified missing transitions by establishing closed Q-value loops in correlated alpha and proton decay chains. It is likely there are missing transitions in the decay path from the 456(2) ns isomer, which prevents a firm assignment for the excitation energy of this long-lived state.

4.6.2 The decay path from the 456(2) ns isomer to the ground state.

The 126 keV, 194 keV and 658 keV γ rays above the presumed 8^+ isomer are difficult to characterise due to their irregular structure. In this respect, ^{158}Lu is similar to its $N = 87$ isotones where the decay paths from the higher-lying states to the 8^+ isomer are complex, highly fragmented and often involve low-energy transitions that can only be detected with sensitive LEPS detectors. However, there are similarities with the positive-parity configurations in the isotones formed by coupling the proton $h_{11/2}$ to the $f_{7/2}$ and $h_{9/2}$ configurations [55, 56, 57, 60].

4.6.3 The high spin states above the 456(2) ns isomer.

There are some similarities with the high-spin states in ^{158}Lu and the sequences built on the 11^- states in lighter $N = 87$ isotones. For example, the ^{152}Tb [60] and ^{156}Tm [55] isotones have 11^- state lifetimes of 4 ns and 400 ns, respectively, and the band head fed by the 405 keV γ ray lies in this range. There are also resemblances between the yrast sequence in ^{158}Lu and the γ-ray cascades built upon the 11^- states in the lighter isotones, see Figure 4.22. These configurations are interpreted to arise from coupling the $h_{11/2}$ proton and $i_{13/2}$ neutron orbitals [55, 56, 57, 60].

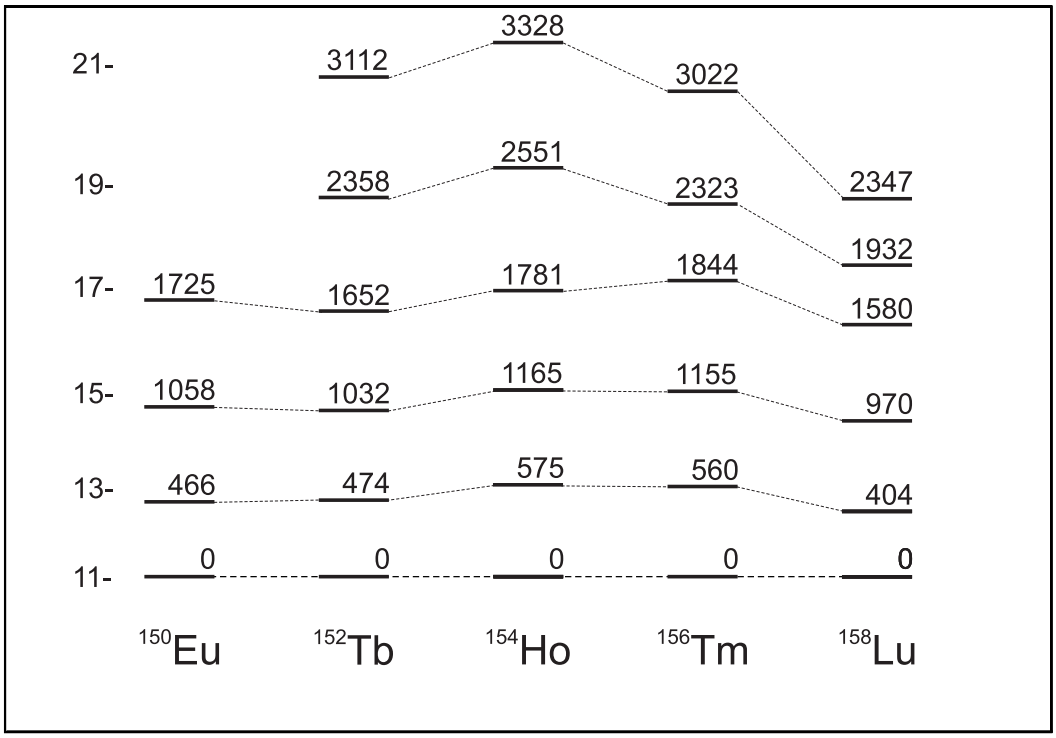

Figure 4.22: Excitation energy level systematics of the $(\pi h_{11/2})^n \otimes (\nu i_{13/2})^m$ configurations above the 11^- states in the $N = 87$ isotones.

The excitation energies of the 13^-, 15^- and 19^- states vary smoothly as a function of increasing proton number. The higher spin states show a trend towards lower excitation energies for the heavier isotones indicating a change in their structure.

Thus, the yrast states above the 11^- state in ^{158}Lu are assigned as the $\pi h_{11/2} \otimes \nu i_{13/2}$ configuration.

Chapter 5

Summary

Excited states in the odd-odd nuclei ^{156}Lu and ^{158}Lu have been identified using selective tagging techniques in conjunction with the JUROGAM II and GREAT spectrometers and the RITU gas filled separator at the University of Jyväskylä Accelerator Laboratory. The present study of the odd-odd nucleus ^{156}Lu has revised and extended the level scheme to high spin and excitation energy. Configuration assignments have been made on the basis of likely multiple quasiparticle excitations that can be generated from the proton and neutron orbitals near to the Fermi surface. The new (19^-) isomeric state at an excitation energy of 2598 keV relative to the 10^+ state is assumed to have a similar character to the high-spin isomers observed in the other $N = 85$ isotones. The isomer de-excites via the emission of a 923 keV γ ray to the 16^+ state with a measured half-life of 120(17) ns and is assigned to have a $\pi h_{11/2}^{-3} \otimes \nu f_{7/2} h_{9/2} i_{13/2}$ configuration.

A 683 keV transition has been observed to be in coincidence with the $(14^+ \rightarrow 12^+)$ and other higher lying transitions but not with the $(12^+ \rightarrow 10^+)$ transition. This γ ray is assumed to be the $(11^+ \rightarrow 9^+)$ transition from the $\pi h_{11/2} \otimes \nu f_{7/2}^3$ multiplet that forms a parallel decay path to the 745 keV transition. Previous research into $N = 85$ isotones has revealed a systematic reduction in excitation energies of

10^+ state built upon the $\pi h_{11/2} \otimes \nu h_{9/2}$ configuration relative to 9^+ state built on the $\pi h_{11/2} \otimes \nu f_{7/2}$ configuration with increasing proton number. This provides a reason for the non-observation of low-energy linking transitions between the yrast structures and the α-emitting 9^+ state.The lowest four quasiparticle configuration above spin 16^+ is presumed to be the $\pi h_{11/2} \otimes \nu f_{7/2} h^2_{9/2}$ state at 17^+. The cascades feeding the tentative 17^+ state could be formed by breaking a $\pi h_{11/2}$ pair and coupling to one or more neutrons into the $\nu i_{13/2}$ orbital; the $\pi h^3_{11/2} \otimes \nu h^2_{9/2} i_{13/2}$ configuration could give rise to a 23^+ state while higher spin states up to 29^+ could be achieved with the $\pi h^3_{11/2} \otimes \nu h_{9/2} i^2_{13/2}$ configurations. The 831 keV transition above the 29^+ state is likely to be a pair-breaking transition to an excited six quasiparticle configuration.The full alignment of six valence particles in the $\pi h^3_{11/2} \otimes \nu f_{7/2} h_{9/2} i_{13/2}$ configuration is expected to produce a state with spin and parity 27^- as observed in the nearby $N = 85$ isotones. The level scheme above the assigned 27^- state splits into three branches involving high-energy γ ray transitions. A mechanism for generating even higher spins by breaking more pairs of $h_{11/2}$ protons and aligning their angular momenta with the neutrons remaining in $\nu f_{7/2}$, $\nu h_{9/2}$ and $\nu i_{13/2}$ orbitals is likely.

A level scheme has been established in ^{158}Lu for the first time. A low-lying 456(2) ns isomer has been identified and assigned to be the 8^+ state based on the $h_{11/2} \otimes [\nu(f_{f/2})^3]_{5/2}]$ 8^+ configuration based on similarities with the lighter $N = 87$ isotones. Two γ rays at 76 keV and 170 keV form part of the decay path from the isomer to the 2^- ground state. The 76 keV transition has been assigned as an electric dipole $1^+ \rightarrow 2^-$ transition on the basis of internal conversion coefficients extracted from intensity balances and K X-ray yields. The 170 keV transition is consistent with an E2 transition depopulating the 456(2) ns isomer however it is apparent that there may be missing transitions in the decay path.

The high-spin level scheme above the 456(2) ns isomer has been established

through three-fold γ-ray coincidences detected in the JUROGAM II spectrometer with the additional constraints of delayed coincidences with the 76 keV and 170 keV transitions detected at the focal plane. Relative intensity measurements indicate the presence of a short-lived ($\sim$10 ns) isomer fed by the high-spin yrast sequence. Thus, the yrast sequence is assumed to be a $\pi(h_{11/2})^n \otimes \nu(i_{13/2})^m$ configuration based upon a short-lived 11^- isomer as observed in the lighter $N = 87$ isotones.

The presence of isomeric states in these odd-odd Lu isotopes provides some scope for future investigations into competing proton-emission branches from excited states. While it is anticipated that γ-ray emission is likely to remain the dominant decay mode, valuable limits on the competing proton radioactivity decays from excited states could be established with a more appropriate experimental set-up.

Bibliography

[1] DT Joss *et al. Phys. Let. B*, 641:34, 2006.

[2] NNDC. http://www.nndc.bnl.gov/chart/. Accessed: 2014-03-15.

[3] ES Paul *et al. Phys. Rev. C*, 51:78, 1995.

[4] KY Ding *et al. Phys. Rev. C*, 64:1, 2001.

[5] M Wang *et al. Chinese Phys. C*, 36:1603, 2012.

[6] CF von Weizsäcker *et al. Z. Physik*, 96:431, 1935.

[7] O Haxel *et al. Phys. Rev.*, 75:1766, 1949.

[8] JE Mayer *et al. Chem. Phys.*, 20:1057, 1952.

[9] JE Mayer *et al.* On closed shells in nuclei. II. *Physical Review*, 75(12):1969, 1949.

[10] RF Casten. *Nuclear Structure from a Simple Perspective.* Oxford University Press, 2005.

[11] SG Nilsson *et al. Mat.-fys. Medd.*, 29:1, 1955.

[12] DL Hill and JA Wheeler *et al. Phys. Rev.*, 89:1102, 1953.

[13] J Suhonen *et al. From nucleons to nucleus.* Springer-Verlag, Berlin, 2007.

[14] BRICC. http://bricc.anu.edu.au/. Accessed: 2013-07-01.

[15] G Gamow *et al. Z. Phys*, 51:204, 1928.

[16] RW Gurney and EU Condon *et al. Nature*, 122:439, 1928.

[17] H Geiger and J Nuttall. *Philosophical Magazine*, 22, 1911.

[18] JO Rasmussen *et al. Phys. Rev.*, 113:1593, 1959.

[19] H Hubel. 51:1, 2005.

[20] DR Rudolph *et al. Phys. Rev. Lett.*, 89, 2002.

[21] IH Lazarus and DE Appelbe *et al. IEEE*, 48:67, 2001.

[22] CW Beausang and J Simpson *et al. Journal of Physics G-Nuclear and Particle Physics*, 22:527, 1996.

[23] RD Page *et al. Nucl. Instrum. Methods A*, 204:634, 2003.

[24] Light Ion Spectrometer Array. http://ns.ph.liv.ac.uk/ dod/LISA/home.html. Accessed: 2014-05-10.

[25] G Duchene *et al. Nucl. Instrum. Methods Phys. Res. A*, 432:90, 1999.

[26] CW Beausang *et al. Nucl. Instrum. Methods Phys. Res. A*, 313:37.

[27] Jurogam II detector angles. https://www.jyu.fi/fysiikka/en/research/. Accessed: 2014-04-01.

[28] J Uusitalo *et al. Nucl. Instrum. Methods B*, 204:638, 2003.

[29] M Leino *et al. Nucl. Instrum. Methods Phys. Res. B*, 99:653, 1995.

[30] M Leino J Saren, J Uusitalo and J Sorri. *Nucl. Instrum. Methods Phys. Res. A*, 654:508, 2011.

[31] PJ Nolan and JF Sharpey-Schafer. *Reports on Progress in Physics*, 42:1, 1979.

[32] D Radford *et al. Nucl. Instrum. Methods A*, 361:297, 1995.

[33] P Rahkila *et al. Nucl. Instrum. Methods A*, 595:637, 2008.

[34] S Hofmann *et al. z. Phys. A*, 333:107, 1989.

[35] RD Page *et al. Phys. Rev. C*, 53:660, 1996.

[36] GD Alkhazov *et al. Z. Phys. A*, 295:305, 1980.

[37] KS Toth *et al. Phys. Rev. C*, 27:889, 1983.

[38] GD Dracoulis *et al. Proceedings of the International Conference of Nuclear Structure at High Angular Momentum, Ottawa, and AECL Report No 10613, Chalk River (unpublished)*, 2:94, 1992.

[39] OB Tarasov and D Bazin. *Nucl. Instrum. Methods*, B204:174, 2003.

[40] T Enqvist and J Uusitalo *et al. Nucl. Instrum. Methods B*, 126:344, 1997.

[41] M Leino and J Äystö *et al. Nucl. Instrum. Methods B*, 99:653, 1995.

[42] RD Page *et al. Phys. Rev. C*, 53:660, 1996.

[43] AF Saad *et al. Z. Phys. A*, 351:247, 1995.

[44] S Andre *et al. Nucl. Phys. A*, 575:155, 1994.

[45] M Piiparinen *et al. Z. Phys. A*, 300:39, 1981.

[46] G Duchene *et al. Z. Phys. A*, 350:39, 1994.

[47] M Piiparinen *et al. Z. Phys. A*, 290:337, 1979.

[48] C Foin *et al. Z. Phys. A*, 305:81, 1981.

[49] C Foin *et al. Eur. Phys. J*, 14:7, 2002.

[50] R Carroll. PhD thesis, University of Liverpool, 2012.

[51] S Andre *et al. Nucl. Phys. A*, 575:155, 1994.

[52] RJ Carroll *et al. Phys. Rev. C*, 93, 2016.

[53] JQ Xu *et al. Phys. Rev. A*, 49:2191, 1994.

[54] HL Hagedoorn and AH Wapstra *et al. Nucl. Phys.*, 15:146, 1960.

[55] H Sun *et al. Z. Phys. A*, 352:115, 1995.

[56] T Komatsubara C-B Moon and K Furuno *et al. Phys. Rev. C*, 88, 2013.

[57] SJ Chae *et al. Z. Phys. A*, 350:89, 1994.

[58] RB Firestone. *Table of Isotopes.* John Wiley & Sons, 1996.

[59] CT Zhang *et al. Phys. Rev. C*, 54, 1996.

[60] C Foin D Barneoud, JA Pinston and E Monnand *et al. Z. Phys. A*, 341:69, 1983.

[61] IG Darby *et al. Phys. Lett. B*, 695:78, 2011.

[62] MC Drummond *et al. Phys. Rev. C*, 89, 2014.